Department of Physics and Astronomy
University of Heidelberg

Master thesis
in physics
submitted by
Ingrid Maria Dippel
born in Frankenberg (Germany)
February 2022

Development and Realisation of a Transportable Cold Atom Machine

This master thesis has been carried out by
Ingrid Maria Dippel
at the
Kirchhoff-Institute of Physics
under the supervision of
Prof. Dr. Fred Jendrzejeweski

ABSTRACT

Transportable cold atom experiments open up a new path for applications in e. g. geodesy, where the differential gravitational red shift can be measured by comparing two spatially separated atomic clocks.

This thesis describes the design and set-up of a transportable cold atom experiment. Furthermore, the stability, performance and reliability of the electronical, optical and mechanical components before and after transport were investigated.

The machine consists of two standardised 19-inch racks, where one is designated for electronical devices. The second one is home-built and features four retractable drawers for mounting optical elements, the $\lambda = 767\,\mathrm{nm}$ laser and the vacuum system.

After completing the full set-up at the University of Heidelberg, the experiment was partially disassembled, transported to and reassembled at a server room at the European Honda Research Institute in Offenbach (Main) within 20 hours. Controlling and observing the experiment fully remotely, we were able to achieve and characterise a two-dimensional magneto-optical trap for $^{39}\mathrm{K}$ atoms in both locations.

ZUSAMMENFASSUNG

Transportable Experimente mit kalten Atomen eröffnen viele neue Anwendungsmöglichkeiten wie beispielsweise in der Geodäsie, wo die differenzielle Rotverschiebung durch zwei örtlich getrennte Atomuhren gemessen werden kann.

Diese Arbeit beschreibt die Entwicklung/Konzeptionierung und den Aufbau eines solchen transportablen Experimentes. Des Weiteren untersuchten wir die Stabilität, Performance und Zuverlässigkeit der elektronischen, optischen und mechanischen Komponenten vor und nach dem Transport.

Der Aufbau besteht aus zwei 19-Zoll Racks, von denen eines für die Elektronik vorgesehen ist. Das zweite ist eine Spezialanfertigung und verfügt über vier ausfahrbare Schubladen für die Montage optischer Elemente, den $\lambda = 767\,\mathrm{nm}$ Laser und das Vakuumsystem.

Nach der Fertigstellung des Aufbaus an der Universität Heidelberg, wurde das Experiment für den Transport zu einem Serverraum des European Honda Research Institute in Offenbach (a. Main) innerhalb von 20 Stunden teilweise abgebaut, transportiert und dort wieder aufgebaut. Indem das Experiment vollständig aus der Ferne steuerten und beobachteten, konnte eine zweidimensionale magneto-optische Falle für $^{39}\mathrm{K}$ Atome an beiden Standorten realisiert und charakterisiert werden.

CONTENTS

ACRONYMS

AOM Acousto-optical modulator

BAAS British Association for the Advancement of Science

BEC Bose-Einstein condensate

CF ConFlat (a standard for the size of vacuum flanges)

CMOS Complementary metal-oxide semiconductor

DFB diode Distributed feedback diode

EOM Electro-optical modulator

EDFA Erbium-doped fibre amplifier

FPGA Freely programmable gate array

GPS Global Positioning System

GUI Graphical user interface

HRI Honda Research Institute

MOT Magneto-optical trap

PBS Polarising beam splitter

PD Photodiode

PDmon PD monitoring board

PID controller Proportional–integral–derivative controller

PM Polarisation maintaining

PPLN Periodically poled lithium niobate

RF Radio frequency

SAS Saturated absorption signal

SI International system of units

Tctrl Temperature controller for heating bands

THsen Temperature and humidity sensor

(U)HV (ultra) high vacuum

VCO Voltage controlled oscillator

1 INTRODUCTION

At the start of last century, when looking for solutions for phenomena not being explainable by classical physics alone, intriguing theories and thought-experiments about the quantum-natured reality we live in were researched and discussed by various scientists like Max K. Planck and Albert Einstein. In the mid 20s, these beginnings were further developed by Niels H. D. Bohr[1], Erwin R. J. A. Schroedinger[2], Werner K. Heisenberg[3] to only name a few to form a unified theory of quantum mechanics.

With the invention and realisation of the first laser in 1960 by Theodore H. Maiman, Charles Hard Townes and Arthur Leonard Schawlow[4], the modern age of experimental quantum science could finally be called on, allowing scientists the precise measurement and manipulation of (sub-)atomic properties. Honoured with the Nobel Prize in 2001, Wolfgang Ketterle, Eric A. Cornell and Carl Wieman achieved the experimental realisation of a Bose-Einstein condensate (BEC) at the Massachusetts Institute of Technology (MIT)[5], cooling atoms down to just a few nK, which "fuse" into a single quantum mechanical entity describable by a single wave function.

Magneto-optical traps (MOT) are one of the most important preceding stages when it comes to cooling down atoms until they reach this "fifth state of matter". Although BECs already offer a huge area of research ranging from quantum material research to implementing quantum algorithms in optical lattices, they have gained in popularity with quantum sensing devices. While some exploit all of the particular properties of BECs, some experiments only require cold atoms as can be found inside a MOT. Examples for both type of experiments are given below.

VACUUM METROLOGY Measuring and controlling vaccua at ultra-high vacuum (UHV) levels is not compelling for scientific research only, but is also a point of great interest for semiconductor fabricators, who are manufacturing microchips laying down ultrathin layers of chemicals in chambers operating at a billionth part of normal pressure.

With the developement of a miniaturised version of an optical trap for atoms, researchers at the National Institute of Standards and Technology (NIST) are able to deploy their device onto other vacuum set-ups in order to characterise their vacuum[6]. These methods may therefore replace older technology e. g. pressure/ion gauges for vacuum measurements and push the international effort to base our In-

ternational System of Units (SI) on fundamental, invariant constants and quantum phenomena, as was already achieved for the SI-second as shown below.

ATOMIC CLOCKS For most history of humankind, macroscopic observables were the base of time-keeping although the technology and definitions relying on their precision and consistency improved over the years. About 150 years ago, the basic unit of time of most scientific measurement systems (e. g. CGS, MKS) was defined as a fracture - $\frac{1}{86,400}$ - of a mean solar day as declared by The British Association for the Advacement of Science (BAAS)[7].

Only a few years later in 1879 Lord Kelvin suggested using atomic transitions lines for measuring time, although the first precise cesium-based atomic clock was to be built 70 years later. After the invention of quartz crystal oscillator clocks in October 1927 by Joseph W. Horton and Warren A. Marrison at Bell Telephone Laboratories[8], devices driving the silicon-dioxide (SiO_2) crystal with a frequency of $f = 32768\ Hz = 2^{15}\ Hz$ ensured an accuracy of already $6 \cdot 10^{-8}$ in the late 1940s. Although this method of measuring time was not yet introduced as an international standard.

In the mid-fifties of last century, the precision of the second was extended by using the solar year as a base since the Earth's orbit around the Sun is far more stable that its rotation around its own axis. However, this meant one still had to rely on macroscopic observables[9]. Around this time, Louis Essen and Jack Parry achieved the first contruction of an atomic clock at the National Physical Laboratory in the United Kingdom in 1955. Making use of the fundamental work of Isidor Rabi on magnetic resonance[10], both scientists claimed to reach precision of 10^{-9} and more[11].

With laser technology arriving in the early 60s the modern era of timekeeping could finally be called on. Precise manipulation and measurement of atomic states enables physicists at various research centres to reach individual measurement uncertainties of a few 10^{-17}[12]. That's why the urge to compare optical clocks directly in order to exploit their full accuracy gives rise to the motivation in making them transportable. Currently, comparisons can be realised via fibre links[13], however the development of transportable clocks would be of great interest for extraterrestial as well as terrestrial applications as shown in the next paragraph.

GRAVIMETRY AND GEODESY One of Albert Einstein's most prominent insights into our reality concerns phenomena like gravitational redshift, deflection of light by curved space-time and time dilation[14]. His model predicts that time goes by more slowly when in proximity of a source of gravitation and passes more quickly when the clock is getting away from the source of gravitation. The first of the three was

experimentally proved by Joseph C. Hafele and Richard E. Keating in October 1971[15] by comparing three different cesium-based clocks of whom one travelled around the world eastwards, the other westwards and the third clock stayed at the United States Naval Observatory. In addition to time-shifts due to gravitational differences, the flight by plane also changes the kinematic properties of the reference frames of the three clocks. In the end, the eastward clock was almost $\Delta t_{east} = 60\ ns$ retarded and the westward clock $\Delta t_{west} = 270\ ns$ advanced with respect to the stational clock.

Modern experiments making once again use of laser technology inaccessible before, are already able to measure gravitational differences in samples of $\Delta d = 1\ mm$ size[16]. This was achieved at the JILA, where scientists used a Bose-Einstein condensate elongated along the gravitational direction towards the earth's core (z-axis). Manipulating the sample with resonant light, the team measured the fraction of excited atoms along the z-axis and could see it shifting linearly, since vertically neighbouring sites are detuned by gravity. Determining the resonance-shifted frequency as a fraction of the original frequency with an accuracy of 10^{-20}, results in a gravitational gradient of $-9.8 \cdot 10^{-22}/mm$.

These high-precision measurements find application in the vast area of geodesy. In geodesy, the geometrical shape, gravitational field of the earth and its orientation in space is measured as accurately as possible. With methods like Global Positioning System (GPS) and gravitational wave detection, research in geodesy helps us to understand the flow of ground-water, detects minerals below the earth's surface and provides important insights for civil engineering of e. g. bridges, dams and skyscrapers[17]. One of the most challenging aspects of geodesy is to design and build highly-accurate atomic clocks, make them transportable to move them to potentially remote locations (e. g. the rim of an active volcano or space) and find means to compare them to other clocks[18][19].

WHY TRANSPORTABLE 19-INCH RACKS ? Since all examples discussed so far already motivate us to think about making a cold atom experiment transportable, this question does not seem to be arbitrary anymore. Even though one's cold atoms experiment gains no physically interesting data from being removed to another location or being still operable on the move, there are still many advantages of the set-up presented in this thesis.

One of the major reasons for this is the possibility of running an experiment at a location, where a much more stable environment may be provided than in a laboratory at an institute. Nowadays, big data centers, whose operators have increasingly shown interest in applying cold quantum devices for their own use, grant temperature controlled and vibration protected server rooms. Next to ultrafast con-

nectivity to the internet as well the ability to host devices with a high drain of electrical power, these facilities might just be the setting for running quantum devices in a safe and secure manner. Also granting the option to move an experiment around in the same building provides a major improvement to flexibility.

Additionally, the attempt to expand an optical experiment to the vertical saves precious space on the horizontal and lets the user access all elements of the experiment with ease. The decision to use a standardised 19-inch rack as a fundamental framework is justified with the fact that most electronic and recently optical components as well are designed to be fastened into these industrial widespread conventions.

Lastly, imagining not only to transfer the experiment to a remote location but continue to operate on the transport still, offers a whole new area of research as shown with mobile accelero-/gravimeters.

THESIS OVERVIEW

- In chapter 2, the theoretical foundations of interaction of (laser) light with atoms will be reviewed. Starting with the most basic case of light scattered by a simple two level atom this chapter explains all relevant, more advanced trapping and cooling schemes deployed in the course of achieving a three-dimensional trap of cold atoms. Furthemore, this chapter includes basic laser physics and a detailed view on ^{39}K.

- Chapter 3 gives an overview of the experimental set-up, starting with the generation and manipulation of the light required for above mentioned techniques. Before going through all the different paths shifting the frequency of the laser by the appropriate amount, our scheme for locking its output frequency will be looked at. In the second section, the vacuum system with all the different chambers and the pumping down process is explained.

- Chapter 4 explains how we achieved making the NaKa-experiment transportable, easy to set up at a remote location and fully controlable by means of an independent connection to the internet. This chapter includes the hardware compositions as well as the networking scheme and its control by the DjangoControlServer.

- Finally, chapter 5 guides through all the preparation and processes for accomplishing the trapping of ^{39}K atoms in a two-dimensional cloud. Here, all experimental results of this thesis are displayed.

- In the last chapter of this thesis, the overall experimental results are evaluated by having a look at the emerging challenges and

how they were overcome. Finally, a brief outlook on further developments is given.

2

FUNDAMENTALS

In order to manipulate and measure atomic properties in a precise way, atoms need to be spatially confined. For this, they must be slowed down and trapped. This can be realised by making use of atom-light interactions described in this chapter. In the last section a short introduction on basic laser physics will be given as well.

2.1 INTERACTIONS OF ATOMS WITH LIGHT

2.1.1 *Rabi Oscillations*

In order to understand the interaction of atoms and light, we reduce our atom to a two-level system. It can be in the ground state $|g\rangle$ with energy $E_g = \hbar \cdot \omega_g$ or the excited state $|e\rangle$ with energy $E_e = \hbar \cdot \omega_g$ such that the energy required to excite the atom is $\Delta E = E_e - E_g = \hbar \cdot \omega_0 > 0$. Its Hamiltonian is[20]:

$$H_{atom} = \frac{\hbar}{2} \begin{bmatrix} \omega_g & 0 \\ 0 & \omega_e \end{bmatrix} \tag{1}$$

The excitation of the atom can be made possible by absorbing a photon of a monochromatic light field, realised for example by a laser, which interacts with the atom. This time-dependent electromagnetic light field is described by $\vec{E}(t) = \vec{e}_x \, E_0 \, \sin(\omega t)$, travelling along the positive x-axis. E_0 denotes the amplitude of the electric field and its frequency is ω, which is identified with the frequency of the photons. Its intensity $I(t)$ is the scalar product of the electrical field with itself such that $I(t) = E_0^2 \cdot \sin^2(\omega t)$. Here, the Hamiltonian for the field in the electric dipole approximation is given by:

$$H_{field} = -\vec{d} \cdot \vec{E}(t) \tag{2}$$

with $\vec{d}$ being the dipole transition operator. The total Hamiltonian describing the interaction of both systems is then given by:

$$H = H_{atom} + H_{field} = \frac{\hbar}{2} \begin{bmatrix} \delta & \Omega_0^* \\ \Omega_0 & -\delta \end{bmatrix} \tag{3}$$

where the *Rabi frequency* $\Omega_0 = E_0 d_e g/\hbar$ was introduced. Furthermore, $\delta = \omega_0 - \omega$ is the detuning of the laser from the atom's transition frequency.

When diagonalizing this Hamiltonian H, one ends up with the frequency

$$\Omega = \frac{1}{2}\sqrt{\delta^2 + |\Omega_0|^2} \tag{4}$$

for the corresponding eigenenergies. Ω is the frequency at which the atom coupled to the light field is forced into the excited state and then back again into the ground state. If $P_g(t)$ is the probability to find the atom in the ground state $|g\rangle$, one obtains Rabi's formula[21]

$$P_g(t) = \frac{1}{1 + \left(\frac{\delta}{|\Omega_0|}\right)^2} \sin^2(\Omega t) \tag{5}$$

and is represented as *Rabi oscillation* in Figure 1. Since the first term is the amplitude of the probability, $(\delta/\Omega)^2$ is a measure for the interaction strength. Note also the shift in frequency for increasing $\delta/|\Omega_0|$.

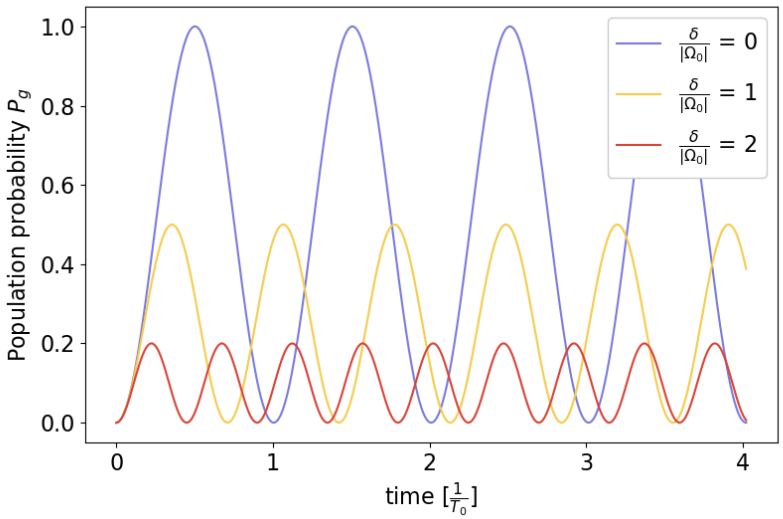

Figure 1: Rabi oscillations for different $\delta/|\Omega_0|$. Note also the shift in frequency.

2.1.2 *Scattering Force*

Additionally to the energy shift, the photon tranfers its momentum onto the atom as it is absorbed. That momentum is $\vec{k} = k \cdot \vec{e_x}$, given the laser beam is propagating along the +x-direction. The atom is pushed into the direction of e. g. a laser beam propagating along the +x-axis consequently. Once the atom is excited to $|e\rangle$, the system can spontaneously fall back to its ground state by emitting a photon of the

exact same frequency $\omega = \omega_0$. This process takes place at the spontaneous emission rate $\Gamma_{eg} = 1/\tau_{eg}$, which is inversely proportional to the lifetime of the excited state τ_{eg}. The photons released by spontaneous emission from the excited state of the atom are distributed randomly over all spatial directions.

This force pushing atoms with the help of light is oftentimes called *scattering force* and is quantitatively described by[22]:

$$F_{\text{scattering}} = \hbar\vec{k} \cdot \frac{\Gamma}{2} \cdot \frac{I/I_{\text{sat}}}{1 + I/I_{\text{sat}} + 4\delta^2/\Gamma^2} \tag{6}$$

Furthermore, the relation $I/I_{sat} = 2\Omega^2/\Gamma^2$ was used, where I_{sat} is the intensity of the light field, at which the rate at which the atoms are excited by photons equals the rate of their scattering rate. The transition is then saturated. When I approaches I_{sat}, the atom is completely subjected to the light field and populates the ground and excited state to equal parts. Mathematically, the last factor of Equation 6 converges against 1 and simplifies to $F_{\text{scattering,sat}} = \hbar\vec{k} \cdot \Gamma/2$, which is then the maximal force one can achieve.

2.2 COOLING ATOMS WITH LIGHT

Since temperature is a measure of the mean kinetic energy of particles, at room temperature atoms averagely move with speed of sound. A mathematical model for noble gases is the *Maxwell-Boltzmann distribution*[23]

$$f(v)d^3v = \left(\frac{m}{2\pi k_B T}\right)^{3/2} e^{-\frac{mv^2}{2k_B T}} d^3v \tag{7}$$

- m particle mass
- k_B Boltzmann constant
- T temperature

such that the mean velocity $\bar{v} \propto \sqrt{T}$. As an example, the average speed of Hydrogen molecules H_2 at room temperature is $\bar{v} = 1100$ m/s while at $T = 1$ K it goes down to $\bar{v} = 65$ m/s and for $T = 10$ nK it reaches values of the order of $\bar{v} \sim 5$ mm/s. In other words, achieving deceleration of the atoms is equivalent to reducing their temperatures, which rectifies the term "cooling". Since temperature is a more intuitive parameter to describe a whole ensemble of many particles, describing them by velocities seems rather unfitting. In order to cool them down and even trap them, one can make use of laser cooling as described above.

2.2.1 *Optical Molasses*

An optical molasses expands the laser cooling to three dimensions by using three counter-propagating laser beam pairs covering all direc-

tions by being directed towards the centre of a trap. To make use of the scattering force effectively, one can use six same-frequency beams oriented such that all are pointing towards a cloud of atoms, covering all three dimensions. If the lasers are red-detuned, only photons of those beams can be absorbed if $\omega_0 = \omega_{laser} + \vec{k} \cdot \vec{v}$ where v is once again the velocity of the atoms. This velocity induced frequency shift seen by the atoms in their centre of mass frame is named "*Doppler* shift" after the physicist, who firstly described this phenomenon in 1842[24].

As a consequence, the atoms are always pushed back to the centre of this light trap until they eventually spontaneously emit photons, gain in momentum because of the recoil force or collide with each other and as a consequence, heat up. These limiting factors set the lower bound for the temperature these atoms may be cooled down to in this configuration to be[25]

$$T_{Doppler} = \frac{\hbar\Gamma}{2k_B} \tag{8}$$

The index *"Doppler"* signifies that this kind of trapping relies on the laser light becoming resonant because of the *Doppler effect*, which makes it a velocity-dependent force. If one looks at only one dimension and the atoms are already significantly slowed down ($|\vec{k} \cdot \vec{v}| << \Gamma$), it has the form[26]

$$F_{scat}(v) = -\alpha \cdot v \tag{9}$$

with $\alpha \propto -\hbar k^2 \frac{\delta}{\Gamma}$. The term for F_{scat} looks exactly like the friction force damping a mechanical oscillator, which is why α is referred to as "light damping coefficient". As the atoms might first oscillate around the focus point of the beams but are then slowed down continuously like a pendulum in viscous liquid e. g. honey, another term for this is *optical molasses*.

2.3 ATOMIC STRUCTURE

Before proceeding with a more delicate trapping scheme, one also has to switch to a more complex atom picture. For explaining magneto-optical traps, fine and hyperfine structures will be introduced in the following. Atoms consist of a positively charged nucleus and a number of electrons, each in a state which is described by a set of numbers - so-called quantum numbers - describing its electrical and magnetical properties. Because electrons as well as nucleons are quantum objects, all of these numbers describe **quantized** physical observables.

The principal quantum number $n = 1, 2, 3...$ denotes the number of the shell an electron is residing in. L, which may range from $0...n-1$ gives information on the electrons azimuthal angular momentum, while the magnetic quantum number $m_l \in [-l, l]$ describes $L_z = \hbar m_l$

the projection of the angular momentum along the z-axis. Lastly, the spin quantum number $m_s = \{-1/2, 1/2\}$ describes the electrons spin, which is an odd multiple of $1/2$ since electrons are fermions.

As the spin of the electron is added to the system, the quantum number L does not describe it sufficiently anymore. One needs to include the coupling of L and S into the quantum number $\vec{J} = \vec{L} + \vec{S}$ which is the total angular momentum of an electron and introduces the *fine*-splitting. This is only an approximation for light elements whereas its calculation gets more complex for heavier ones.

With this, every electronic state can be identified whereas a common nomenclature is as follows : $n\,^{2S+1}(L)_J$, though for L_z instead of numbers, the order of letters s, p, d, f... is used to denote $l = 0, 1, 2, 3...$ (s for *sharp*, p for *principal*, d for *diffuse*, f for *fundamental*...). As such, they obey Fermi-Dirac statistics, which in turn obey *Pauli's exclusion principle*, forbidding electrons or fermions in general to populate one state with a particular set of quantum numbers, if it is already occupied.

However to also include the interaction between electron and nucleon spin I, another quantum number is introduced. $\vec{F} = \vec{I} + \vec{J}$ identifies every *hyperfine* level with a total magnetic quantum number m_F.

2.3.1 *Detailed View on Potassium-39*

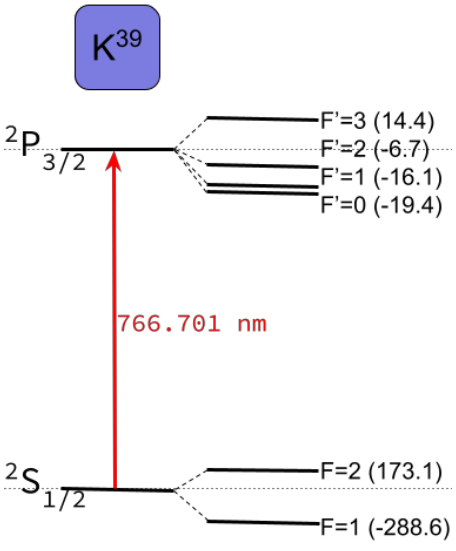

Figure 2: Level scheme of ^{39}K. Offset frequencies given in MHz. Data taken from [27]

The isotope we study is potassium-39. It is well suited for cold atom experiments because of its electron configuration, its stability and abundance in the earth's crust compared to some other alkali metals[28]. Also when in solid form, it is easy to handle when contained in glass ampoules as ingots. With the inner atomic structure introduced in the last section, we will now have a closer look on the specific structure of ^{39}K .

While the atomic number of potassium is 19, meaning that its nucleus contains 19 protons, the atomic mass number "39" indicates that this isotope has one additional neutron, which determines its fermionic nature. It is also the most abundant with a ratio of 93 : 7 compared to the rarer isotopes ^{41}K and ^{40}K[27]. The cooling transition of interest is the D_2-line, which is the electronic transition

between $4^2S_{1/2} \rightarrow 4^2P_{3/2}$ as shown in Figure 2. It has a wavelength of $\lambda = 766.701\,nm$ and therefore falls into the NIR (near infrared) regime of visible light. Whereas the lower level is split up in two hyperfine levels, the upper state is split up in four different levels. Because the coupling of the hyperfine levels to the nuclear spin I is stronger for the $S_{1/2}$ level than for the $P_{3/2}$ level, the splitting of the lower $F = 1$ and $F = 2$ of 400 MHz is almost six times larger than the total splitting of the upper hyperfine levels of about 35 MHz. Typically, it can not be resolved by means of atomic spectroscopy.

Potassium is part of the first main group of the periodic table and being situated in the fourth period means that it has one electron in the fourth s-shell with all lower orbitals being filled up completely. Because all atoms strive to reduce their energy and achieve noble gas configuration, all alkali atoms are highly active and try to find bindings in which they can "transfer" their residual outermost electron to a chemical binding partner. Therefore one may approximate such potassium atoms as a Hydrogen atom, whose nucleus' mass and electric charge is modified by the additional non-reactive electrons, neutrons and protons.

In comparison, the other isotopes ^{40}K and ^{41}K have slightly upshifted levels because the greater number of neutrons additionally and electrons in lower shells shield the positive charge of the protons and thereby weaken the electrical attraction. Note also, that since the number of protons and neutrons for ^{40}K are odd, its nuclear spins I is a half-integer, making this type of potassium a boson. For more information on ^{39}K and the other isotopes, refer to Table 1.

Table 1: Several properties of the potassium isotopes. Data taken from [27]

	K^{39}	^{40}K	^{41}K
Neutrons N	20	21	22
Abundance [%]	93.26	0.01	6.73
lifetime τ	stable	1.28×10^9 y	stable
nuclear spin	3/2	4	3/2
vapour pressure at $T = 293$ K		1.3×10^{-8} mbar	

2.4 MAGNETO-OPTICAL TRAPS

A more advanced trapping scheme involves magnetic fields, which constitute an position-dependent confinement on the trapped atoms. As atomic levels with $m_F \neq 0$ are influenced by external magnetic fields, so are the resonant transition frequencies. This effect is known as *Zeeman* effect and can be mathematically described by[23]

$$\Delta E_{Zeeman} = g_F \cdot \mu_B \cdot m_F \cdot B \tag{10}$$

with g_F, μ_B and B being the *Landé*-factor, the *Bohr* magneton and the absolute magnetic field respectively.

Furthermore, because of selection rules more extensively discussed in various textbooks[23], only light with a certain polarisation may be absorbed and emitted by these magnetically sensitive states. Here, the laser beams propagating in opposite directions are left- (σ^-) and right (σ^+)-handed circularly polarised and may only speak to transitions with $\Delta m = \pm 1$. Imagine now the ground state to be magnetically neutral ($m_F = 0$) as before and the upper sub-states ($m_F = -1, 0, 1$) being affected by a magnetic field gradient generated, linearly increasing with distance from the trap centre. It is generated by two coils in *anti-Helmholtz* configuration. The complete set-up is drawn schematically in Figure 3, where the flow of the current inside the coil, the magnetic field lines and the polarisation of the laser beams are indicated by the black, yellow and red arrows respectively. The coils are driven by two counter-directed currents with a distance

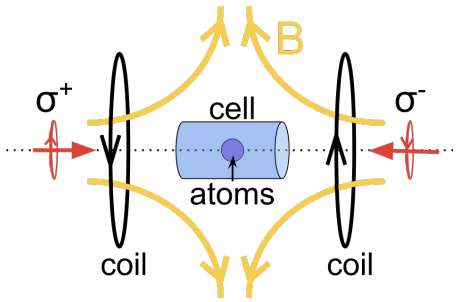

Figure 3: Schematic MOT set-up. Two counter-propagating beams and the mag. field trap the atoms inside a vacuum cell.

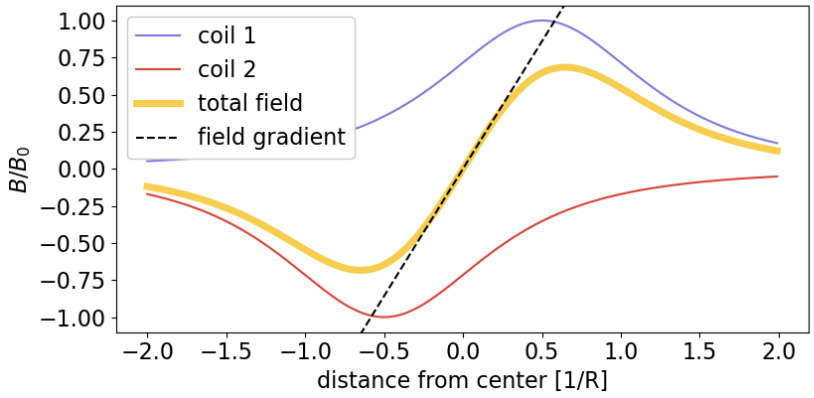

Figure 4: Magnetic field gradient generated by two coils in anti-*Heklmholtz* configuration. B_0 is the maximal magnetic field of one coil.

of R between them, which is equal to their radii. The magnetic field generated by the coils can be seen in Figure 4. If an atom remains within a certain distance from the centre where $B = 0$, no photons are absorbed by it and it stays unaffected by the laser beams. If, however, it leaves the centre e. g.to the right, the upper $m_F = \pm 1$ states begin to shift in energy. In the case depicted in Figure 5, the $m_F = +1$ state is lowered down such that it becomes resonant to the

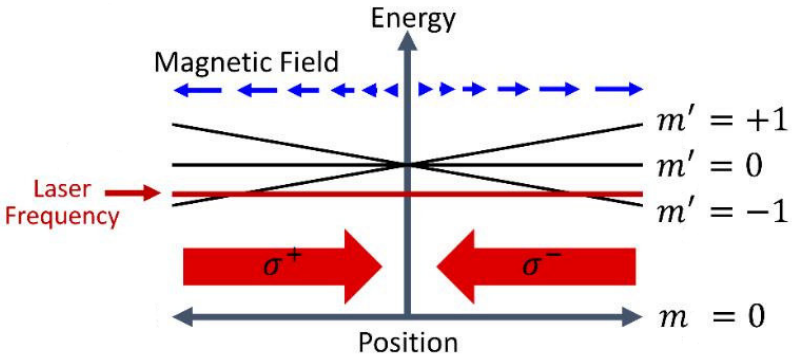

Figure 5: Linear part of the magnetic field gradient (blue arrows) with the upper sub-states being shifted. Figure taken from[29].

red-detuned doppler-shifted σ^+ light coming from the $-x$-direction and is pushed back to the centre due to the scattering force. It works the other way around with σ^- light and the $m_F = -1$ state as well and with this technique, temperatures are now bound from below by the *recoil limit*[30]

$$T_{recoil} = \frac{\hbar^2 k^2}{2Mk_B} \qquad M : \text{mass of atom.} \quad (11)$$

Like with optical molasses, magneto-optical traps can be refined by deploying six laser beams and quandruple magnetic field coils such that the repulsive force discussed above may take effect in all three dimensions.

2.5 BASIC LASER PHYSICS

The transition energies between sub-atomic levels are specific for every isotope of a chemical element. Because of this, atoms may only emit and absorb photons of a certain energy and therefore a certain wavelength. In order to create high-intensity, coherent laser light, one wants to have as many photons as possible emitted at the same time, which can be achieved by **L**ight **A**mplification by **S**timulated **E**mission of **R**adiation, giving the technology its name. The idea is to use a poplulation inversion between two atomic levels of the desired wavelength

$$N_{lower} \ll N_{upper} \quad (12)$$

where the lower level is stable and only sparsely populated by atoms (N_{lower}) and the upper one a meta-stable state and highly populated (N_{upper}). A photon of the respective wavelength passing by then stimulates the atoms in the upper level to fall down to the ground state and thereby emitting photons at the same time. To realise this in practice, usually a four level scheme is deployed where the procedure is as follows[31]:

1. Atoms from the ground state are pumped into a short-lived upper level.
2. From there, the atoms quickly decay with Γ_{upper} to the metastable, which is the upper lasing transition level.
3. Via stimulated emission of already present photons, all atoms are forced to the lower lasing level. The population inversion is now completely spent.
4. At some point, the atoms spontaneously emit radiation at a rate of Γ_{lower} and the electrons start in the ground state once again.

A sketch of the simple two-level as well as the four-level scheme is shown in Figure 6. In this more advanced scheme, two additional levels (the lowest and the highest) are used as a pumping transition to avoid a saturation of the lasing transition (both intermediate levels) by the pump laser. Note however, that the circles are not representing the electrons but the whole atom in their respective energy states.

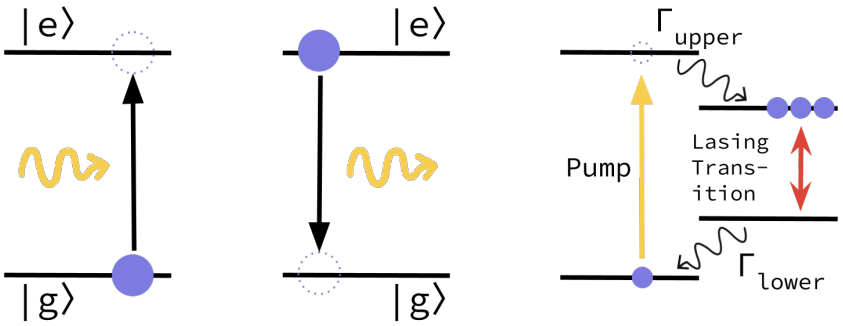

Figure 6: Simplified two-level system and four-level population inversion lasing scheme.

The active diode material hosting the atoms is confined in a cavity of two or more high-reflective mirrors. This narrows down the frequency of the photons being generated by constructive interference, since only those are not eliminated by destructive interference, which obey the standing wave condition:

$$m \cdot \lambda = 2 \cdot n \cdot L \leftrightarrow f_m = \frac{c}{\lambda} = m \cdot \frac{c}{2 \cdot n \cdot L} \qquad m = 1, 2, 3... \quad (13)$$

Here, L is the total path length and n is the refractive index inside of the cavity set-up. As the photons are reflected between the mirrors back and forth several million times in only a part of a second, a huge amount of photons of the same frequency is accumulated. One of the mirrors at which the laser light is leaving the cavity should feature a slightly smaller reflectance than the common value for these applications $R \lesssim 99.9\%$, such that some of the photons are emitted by the diode. The aim is to have a high photon number output while still maintaining a high optical gain inside the cavity.

2.6 SUMMARY

In this chapter we have had a look at a simplified scheme for an atom, which however is already suitable to explain the most important interaction mechanisms with coherent light. Starting with the scattering force, different, more advanced cooling schemes were explained, which are able to further constrain atoms in their kinetic energy as well as spatially.

Introducing the hyper-fine levels of the inner-atomic structure, laid the foundation for the three-dimensional magneto-optical trap, which is one of the main experimental achievements exploited in this thesis. Since all cooling mechanisms require strong, low-noise coherent light, we have also seen how laser light is generated inside a cavity hosting an active medium.

3

EXPERIMENTAL SET-UP

This chapter will show how the previously describes physical phenomena are actually made use of in the experiment. Starting from the light source, a narrow-bandwidth $\lambda = 767\,\mathrm{nm}$ laser, this section will guide through generation, manipulation and redirection of the laser beams to the atoms inside the vacuum system. Next to our spectroscopy and laser locking scheme, frequency modulation techniques as well as the actual physical set-up on the laser table breadboard will be reviewed. In the last section, a brief introduction to vacuum physics and pumps and a presentation of the vacuum set-up will be given.

3.1 LASER

3.1.1 *Laser Set-up*

The laser used is a SML767-211 by the company µQUANS[1]. Physically, the laser's dimensions are roughly $15\,\mathrm{cm} \times 50\,\mathrm{cm} \times 60\,\mathrm{cm}$ (H x B x T) whereas the different opto-electrical components protected by the aluminium cover are shown schematically in Figure 7 (subfigure (a)).

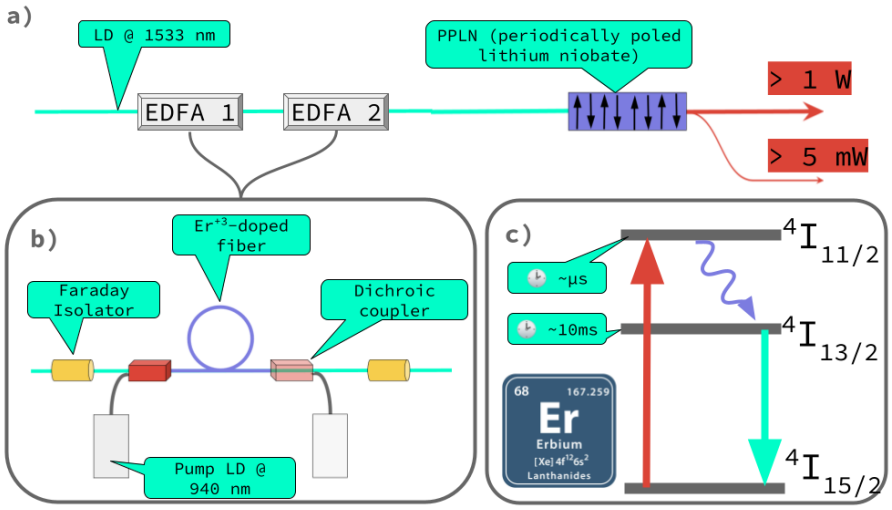

Figure 7: Schematic of the internal electro-optical units (a) and detailled view on the EDFA modules (b). (c) shows a simplified level structure of erbium.

1 https://www.muquans.com/

The light initially generated in the laser diode is of the wavelength $\lambda = 1533\,nm$, which is leaves the gain medium and its cavity coupled to a fibre. Because this light coming out of the laser diode is not used directly, but rather serves as the basis - or "seed" - for the actual output, the laser is called "seed" laser. Two cascades of **e**rbium-**d**oped **f**iber **a**mplifiers (EDFA), which can be controlled individually, amplify the laser light according to the following mechanism: A $\lambda = 940\,nm$ laser pumps the erbuim atoms from the $^4I_{15/2}$ ground state into the short-lived $^4I_{11/2}$ from which they quickly decay into the meta-stable $^4I_{13/2}$ state (see (c) in Figure 7).

By stimulated emission of the photons coming from the laser diode, the erbium atoms decay back into their ground state by emitting resonant $\lambda = 1533\,nm$ photons, amplifing the signal. Afterwards, they are directed towards a **p**eriodically **p**oled **l**ithium **n**iobate (PPLN)[32]. Here the photons are frequency doubled in a nonlinear optical process such that the wavelength becomes $\lambda = 767\,nm$ and is split into two polarisation maintaining (PM) fibres of which one output provides $P_{low} \approx 5\,mW$ and the other $P_{high} \approx 5\,W$ (henceforth called low- and high-power output respectively). Because the high-power output features an output power $P > 500\,mW$, it is categorized as a class IV seed laser has a linewidth as narrow as $\Delta f = 40\,kHz$.

3.2 LASER LOCK

The laser's output is prone to vibrations, changes in humidity and especially temperature variations. Although current technology allows for the world's most stable laser residing at Joint Institute for Laboratory Astrophysics (JILA) to have a thermal noise variation below $2 \times 10^{-16}\,Hz$[33], a scheme must be deployed to set the laser to stay at the desired frequency.

3.2.1 *Saturated Absorption Spectroscopy*

Atomic spectroscopy is an important scheme to get a glimpse at the isotope-specific inner-atomic transition wavelengths and lock our laser to one of these. As the name suggests, light of a certain range of frequencies is applied to the probe, which is in a gaseous form inside a transparent quartz glass or borosilicate cell, and is then analyzed afterwards. While quartz glass cells allow for anti-reflecting coating for the windows, our set-up uses the second and cheaper variant. If a frequency is resonant with a transition it is absorbed by the probe atoms. This absorption results in a transmission dip in the measured spectrum.

An example of such a spectrum is shown in Figure 9 as a solid purple line, which shows a broadened absorption line not suitable to be used for laser locking. Furthermore, it is not even centreed around a

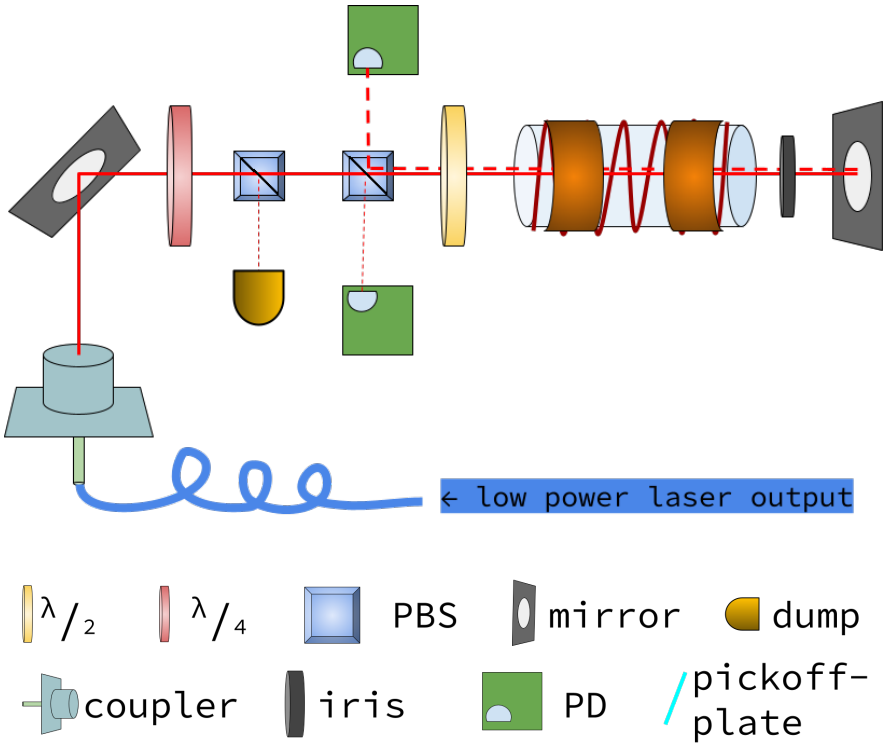

Figure 8: Schematic of the saturated absorption spectroscopy set-up.

transition frequency, but the sum of two transmission dips generated by two different transition frequencies (dashed purple lines). This broadening occurs since the atoms inside the spectroscopy cell are not standing still but move due to their thermal velocity as discussed in Chapter 2. Because of this thermal velocity, the laser frequencies are doppler shifted and the absorption profile broadened in the frequency domain.

A trick to avoid this issue is to use two counter-propagating laser beams that both interact with the atoms. The resulting absorption dips in the spectrum are doppler-free, which can be achieved with the set-up shown in Figure 8 as it is deployed in the experiment discussed in this thesis. First of all, the beam passes a $\lambda/2$ plate and then cleansed by a first polarising beam splitter/cube (PBS). A beam dump catches all reflected light. At the second cube, the light should pass through completely and enters the vapour cell after passing a $\lambda/4$ plate. Although the incoming light is already correctly polarised and cleansed, a photodiode (PD) at the second PBS can give an account of unwanted polarisation fluctuations remaining at the second cube still. Since this signal never exceeded a few μV, a satisfactory polarisation can be assumed. The red spiral around the cell symbolises a copper coil, which in reality has about $n = 100$ windings, while bandheaters are depicted by the two thicker bands enclosing the cell. After the beam is reflected at the other end of the cell and reduced in power, it passes the cell from the other direction and once again the $\lambda/4$ plate.

Because of this, the retro-reflected beam has the opposite linear polarisation and is reflected at the second PBS and directed towards a photodiode.

The incoming laser beam is high in power is called "pump beam" and scans the area of interest with a bandwidth of about $\Delta\omega = 500\,\mathrm{MHz}$. Here, it drives the transition of the D_2-line of ^{39}K at $\lambda = 767.701\,\mathrm{nm}$. The retro-reflected or "probe" beam, that is lower in intensity, counterpropagates the pump beam in the cell and is read out.

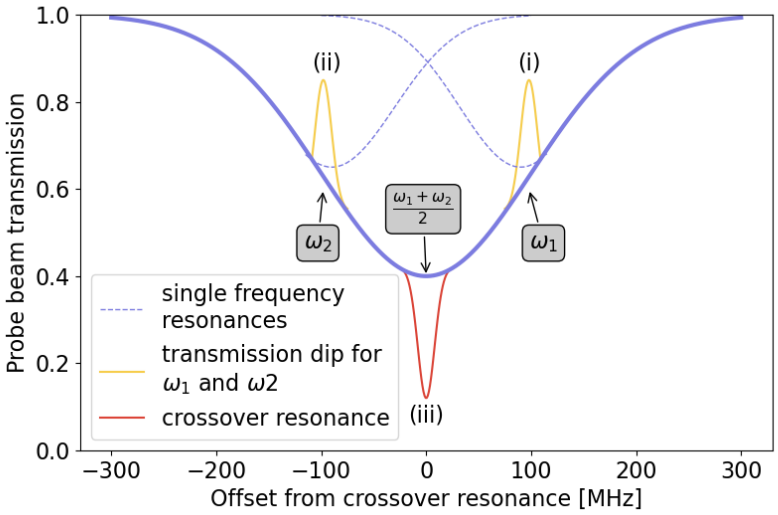

Figure 9: Doppler broadened profile (purple) of both resonances, transmission peaks (yellow) for ω_1 and ω_2 and dip (red) for crossover resonance

Without the pump beam and for an atom with two upper and one ground state, the signal of the probe beam here would look exactly like one of the dotted lines as shown in Figure 9 : a doppler broadened gaussian profile centred around the atomic resonance frequencies ω_1 or ω_2. The result of both profiles is given by the thick solid line.

If now the laser is currently running at the frequency $\omega = \omega_{1/2} + \Delta\omega$, the atoms with longitudinal velocity/velocity parallel to the laser beam $v_{||} = c \cdot \Delta\omega/\omega_{1/2}$ may be addressed by the first so-called *pump* beam, whereas the weaker *probe* beam affects those with velocity of $-v_{||}$. Thus for $\omega \neq \omega_{1/2}$, the spectrum for the probe beam is unaffected in presence of the stronger first beam. On the other hand side, if $\omega = \omega_{1/2}$, the atoms with $v_{||} = 0$ are susceptible for both counterpropagating beams and since most of them are already saturated by the *pump* beam, the *probe* beam is transmitted and its spectrum shows a peak at the resonance as yellow lines as shown in Figure 9.

For potassium, resonances are found for $F = 1 \rightarrow F'$ ($\omega_{F=1} = \omega_1$), $F = 2 \rightarrow F'$ ($\omega_{F=2} = \omega_2$) and the crossover resonance, which will be explained in the following paragraph. Additionally, the three dif-

ferent cases are represented in a drawing in Figure 10, where the thicker and slimmer arrows represent the pump and probe beam respectively.

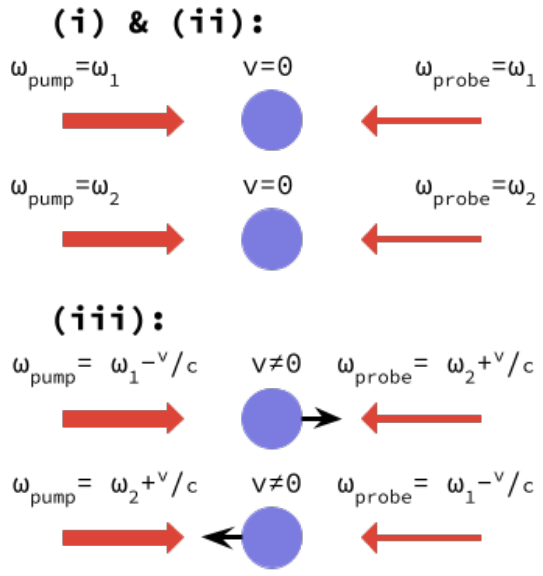

Figure 10: Schematic of the three different cases labelled in Figure 9.

CROSSOVER RESONANCES Whereas the upper hyperfine levels of $4^2P_{3/2}$ are typically not resolved by our saturated spectroscopy set-up, features of the electronic transitions from the two lower lying hyperfine states are discernible. Furthermore, an additional feature appears at the centre between those two, the so-called *crossover resonance*. Because the two types of transitions (from $F = 1$ and $F = 2$) of the hyperfine states share a common upper state, this system is referred to as Λ-system while the inverse case, where two distinctive upper states decay to the same lower state is called V-system. Here, atoms with a longitudinal velocity for which $\omega_{F=1} = (1 + v_{||}/c) \cdot \omega$ and $\omega_{F=2} = (1 - v_{||}/c) \cdot \omega$ is true, may be addressed by the blue-shifted probe and the red-shifted pump beam respectively, such that a transmission dip emerges (see Figure 9).

In a V-system, the same principle applies to the opposite case and a transmission peak shows up. The pump beam empties the lower state by exciting atoms to the resonant upper state such that the blue-/red-shifted transition frequency of the probe beam for the other upper state is transmitted.

In Table 1 we have seen that the vapour pressure for potassium at room temperature is of the order of 10^{-8} mbar, which is too low to get a strong signal. This is why the potassium cell is enclosed with two band heaters, which are controlled with an arduino programmed with a PID-loop (Tctrl). A measurement for different heating temperatures is given in Figure 11a. For rising temperatures, the crossover

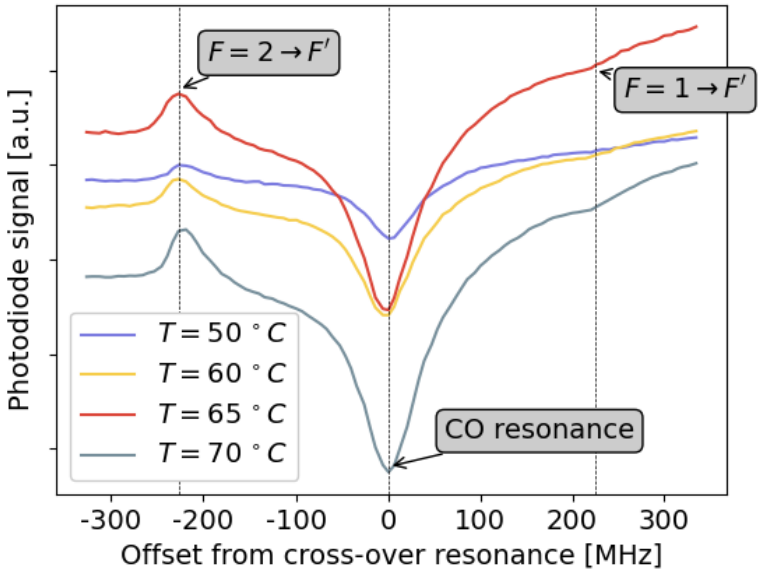

(a) Spectroscopy signal at T $= 50, 60, 65$ °C and 70 °C.

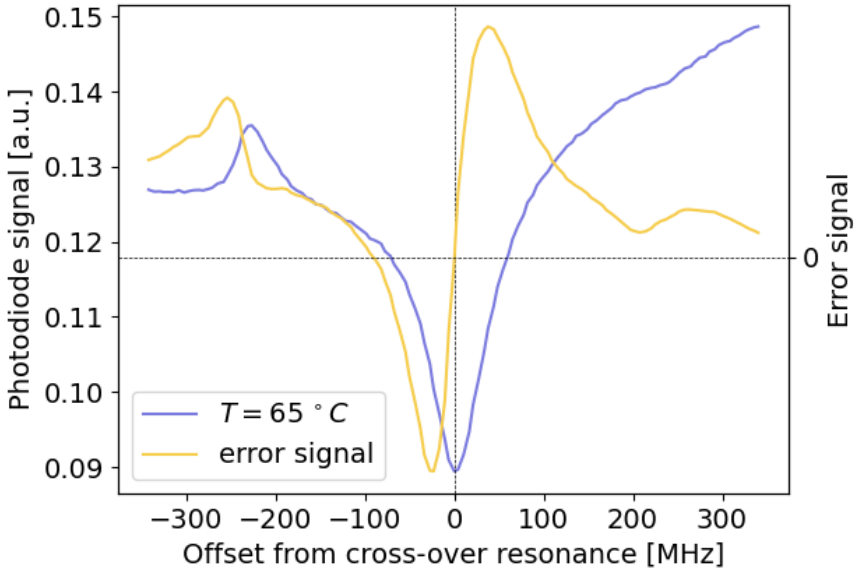

(b) Spectroscopy signal at T $= 65$ °C and the corresponding error signal.

Figure 11

resonance transmission dip as well as the other features are getting more pronounced until temperature reaches 65 °C. Continuing to heat the system, the overall signal strength decreases without any improvement of the transmission features.

Note, that in Figure 11 the feature for the $F = 1 \rightarrow F'$ transmission should be a transmission peak indeed, however it overlaps with the ground state crossover resonance of the ^{41}K isotope at $\Delta\omega \approx 230\,MHz$ offset from the crossover resonance of ^{39}K.

3.2.2 *Locking Scheme*

After having discussed the spectroscopy scheme, which is a necessary tools for locking the laser, we will go through the complete locking scheme step-by-step.

1. The laser is scanned in laser diode current by applying a ramp of amplitude $V_{ramp} = 1\,V$ and a low frequency of about $f_{ramp} \sim 10\,Hz$. This is done with the help of a *STEMlab 125-14*[2]/RedPitaya, a small, multi-tool FPGA (**f**reely **p**rogrammable **g**ate **a**rray) board, featuring two RF (**r**adio **f**requency) inputs and outputs.

2. After centreing the cross-over feature of the SAS spectrum with respect to the ramp, its amplitude is reduced such that only the central dip is visible over the ramping range.

3. The RedPitaya also sends a comparatively high-frequency modulation signal $f_{mod} \sim 10\,kHz$ to a copper coil wound around the spectroscopy cell. The changing current generates an ever-changing magnetic field, which in turn modifies the resonance frequencies of the potassium atoms. As a result, the SAS signal is modulated and an error signal is generated. This error signal is proportional to the first derivative of the original signal and for a depiction of this process refer to Figure 11b above.

   Side Remark: *Since the output of the RedPitaya performs at currents below $I_{RP} = 1\,A$, a current amplifier board is plugged between coil and the FPGA device.*

4. The PID module of the RedPitaya is set to $\mathtt{setpoint} = 0$ (or any value close to zero in case the original signal was not perfectly centreed around the zero-crossing of the ramp), the ramp is turned off and the output of the PID module directed to control the laser instead. The laser is now locked, as long as the error signal is zero. If one did not succeed, the same procedure is repeated with slightly modified locking parameters.

Because the modulation of the SAS spectrum is not performed directly on the laser itself but indirectly through making use of the influence of a magnetic field to the atomic properties of the test gas, the laser bandwidth is not affected by f_{mod}.

2 https://redpitaya.com/stemlab-125-14/

3.2.3 *Frequency Modification*

Having obtained a secure lock of the laser to a certain frequency, one may now start to generate the necessary frequencies to manipulate the atoms inside the vacuum system effectively. For this, we make use of acousto- and electro-optical manipulation, which in turn are based on the wave characteristics of light, especially re- and diffraction.

ACOUSTO-OPTICAL MODULATION Since light exhibits wave characteristics, it can be described by the most fundamental wave equation

$$c = \lambda \cdot f \qquad c : \text{speed of light}, \lambda : \text{wavelength}, f : \text{frequency} \quad (14)$$

To be precise, $c = c_0/n$, where n is the refractive index of the medium the light wave travels through and c_0 as the vacuum speed of light. With help of this and making furthermore use of Equation 14 one receives *Snell's law*[34]:

$$\frac{c_2}{c_1} = \frac{n_1}{n_2} = \frac{\sin(\alpha_2)}{\sin(\alpha_1)}, \quad (15)$$

which also explains how light is refracted when the angle of incidence to the second medium is non-zero. Usually however, not all the light is refracted such that one may observe diffraction as well as shown in Figure 12a. In a simplified view, a crystal is a static, uniform struc-

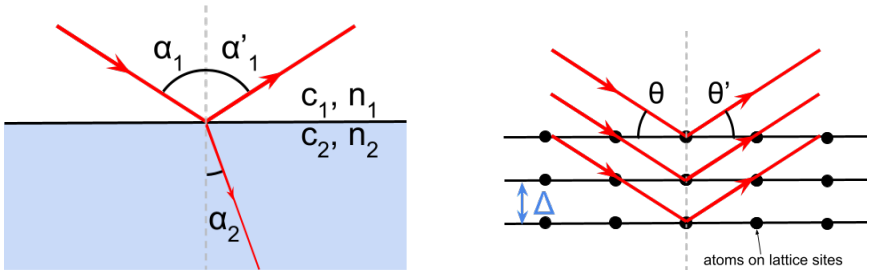

(a) Sketch of a light beam hitting a surface under angle α_1.

(b) Incoming wave vectors being reflected at a crystalline lattice.

Figure 12: Diffraction and reflection of light.

ture with atoms sitting at sites of a two-dimensional, quadratic grid. When Δ is the distance between the different layers of the grid, oftentimes called lattice constant, only those beams being diffracted at the different atomic planes interfere constructively for which

$$n \cdot \lambda = 2 \cdot \Delta \cdot \sin(\theta') \quad (16)$$

is true as depicted in Figure 12b. Because Bragg explored crystalline structures with the help of similarly-scaled X-rays ($\lambda \sim 150\,\mathrm{pm}$), Equation 16 is also-called *Bragg condition* and is depicted in Figure 12b. An

acousto-optical modulator (AOM) such as deployed in the experimental set-up described in this thesis, is essentially a Tellurium Dioxide (TeO_2) crystal block about the size of a match box with a refractive index of $n = 2.25$[35]. When such a crystal lattice is attached to a piezoelectric transducer, it excites a soundwave inside the crystal when driven by a RF driver. Different types of AOMs feature a characteristic centre frequency with a bandwidth ranging from 20 to 40 MHz[36]. The oscillation of the lattice results in a travelling refractive index grating. Typical acoustic wavelengths inside the TeO_2 crystal driven at a frequency of e. g. 100 MHz are $\Lambda \sim 10\,\mu m - 100\,\mu m$, which is effectively the distance between two layers of a higher (or lower) refractive index and replaces the lattice constant Δ in Equation 16. At these lattice constants, even visible light experiences diffraction. Furthermore, the diffracted beam of the *mth* order experiences a shift in frequency, which can be regarded as conservation of energy/momentum when the photons of the laser light interact with the phonons inside the crystal:

$$\Delta f = m \cdot F \qquad F : \text{phonon frequency} \quad (17)$$

In our set-up we are working inside the *Bragg regime* ($L \gg 2 \cdot \Lambda/\lambda$, L : length of the beam path through the crystal) such that the transmitted beam and usually its first two diffraction orders in both directions are visible. AOMs are often used in a double-pass configuration, where the $+1$ (or -1) order is reflected back into the AOM to be diffracted to its original angle of incidence. In this case, the AOM shifts the laser frequency twice - once per passage - and the outgoing laser beam overlaps with the incoming one, making changing the RF frequency afterwards much easier. Figure 13 shows how the light is diffracted when a RF signal is applied or turned off. By orienting the AOM at a

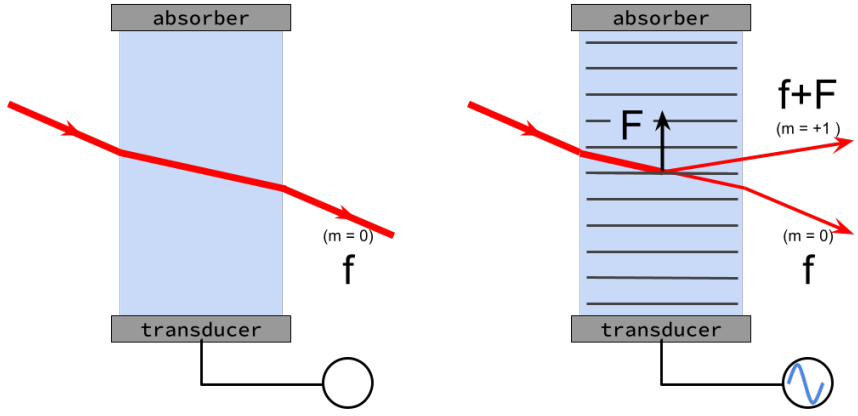

(a) AOM turned off. (b) AOM driven with RF signal.

Figure 13: Acousto-optical modulation by modulating a crystal lattice with RF frequencies.

small angle respective to the incoming beam enables us to maximise the intensity output at the desired minus first order.

ELECTRO-OPTICAL MODULATION The result of frequency shifting light by means of the electro-optical effects is essentially the same as for the acousto-optical effect. Here, the modulation of the refractive index of an optically nonlinear crystal is done by an electrical field having an impact of shifting the layers inside the crystal, parallel to the applied voltage. This phenomenon of the applied voltage having an influecene on the refractive index of a material was first described by Friedrich Pockels in 1906 and is known as *Pockels effect* and can only occur in non-centrosymmetric materials. For the manganese-oxide doped lithium niobate ($MgO : LiNbO_3$) crystal used here, its magnitude is of the order of $30\,pm/V$.

Although being substantially more expensive than AOMs, the biggest advantage for EOMs is the fact that they can shift frequencies by higher amounts with only one transmission and are still resonant to the respective laser light wavelength. Furthermore, the different orders are already overlapped which makes utilisation for the same cloud of atoms and coupling into one common fibre more straightforward.

3.3 LASER TABLE DRAWERS

As discussed in a previous section the laser is locked to the crossover resonance of the potassium D2-line. In the following, we will go through the laser table set-ups as shown in Figure 14. To reduce the beam diameter coming out of the high-power output of the laser, the light is firstly send through a *Galilean telescope*, because the AOMs and EOMs have a limited aperture size. It is then split at a polarising beam splitter (PBS) to be either send to the second drawer or be modified and fibre coupled for usage in the 2D-MOT. The laser light for the 2D-MOT cooling transition ($F = 2 \rightarrow F'$) is sent through a double pass, shifting the frequency by the RF signal of the AOM twice ($\Delta f \approx 2 \times 126\,MHz$), since only the first diffraction order is allowed to propagate by cutting of the 0th order with help of conveniently positioned irises. The EOM is partially shifting the laser light to serve as a repumper ($\Delta f \approx 465\,MHz$). Afterwards, the light is once again (polarisation maintaining (pm)) coupled into two fibres and then directed to the cage systems of the 2D-MOT chamber.

Following the light from the first incoupler to the second drawer, it is sent through two double passes to generate cooling light for the 3D-MOT and the push beam respectively. While the push beam light is ready to be fibre-coupled and used after the double pass, the light for the 3D-MOT has to be modulated by another EOM, generating the repumper frequency, before being split in three and coupled. For

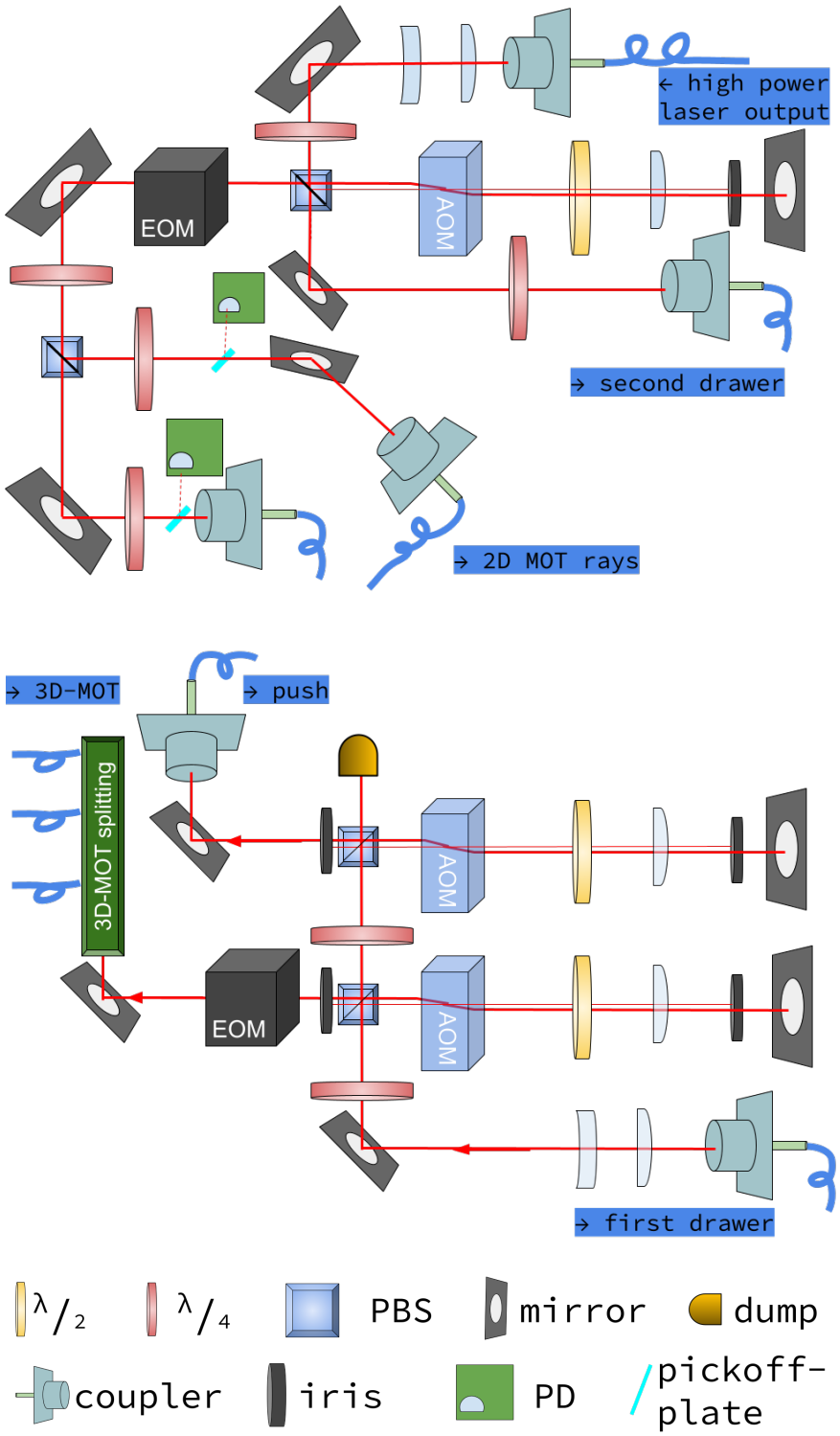

Figure 14: First (top) and second (bottom) laser tables fixed on the drawers.

this we are using a sequence of two PBS with two half waveplates, which control the power ratio of the transmitted and reflected beam, and three incouplers.

In Table 2, all frequencies for the AOMs and EOMs as well as their respective detunings from the transition frequencies and intensities are listed.

Table 2: Detunings of the different light paths.

		f_{AOM} [MHz]	δ [MHz]	I [$\frac{mW}{cm^2}$]
2D-MOT	cooler	−126.8	−44.4	37
	repumper	−98.7	−5.0	37
3D-MOT	cooler	−121.8	−34.4	5
	repumper	−104.2	−16.0	5
PUSH		−126.8	−44.4	6

3.4 VACUUM

So far, we have seen how lasers enable us to manipulate atoms with light scattering forces and a smart way to take advantage of the magnetically susceptible electronic sub-states. In order to deploy laser light on the atoms, the previous part of this chapter showed how the light is first generated and then frequency shifted on two small-sized optical breadboards. All respective light paths are then fibreized such that they can be connected to cage systems, which in turn connect the optical components to the vacuum chambers containing the potassium-39 atoms. The latter and more details on the vacuum system are described, being evidently the core of the whole cold atom experiment.

3.4.1 *Introduction to Vacuum Physics*

Although we have seen ways on how to achieve our goal to manipulate potassium-39 atoms with precisely tuned laser frequencies, this process is nearly impossible to perform under standard conditions. The whole working principle of laser cooling is disturbed by alien atoms and molecules, which are unaffected by the laser beams and may therefore create a "background" of fast moving particles. As a consequence, these will disturb the cooling process by random collisions, continuously adding kinetic energy to the potassium atoms. These unwanted effects can be avoided by performing the preparation and read-out of the experiment under vacuum, whose main property is defined by pressure

$$p = \frac{F}{A} \qquad [p] = \frac{N}{m^2} = Pa \quad (18)$$

quantifying the total collision force F per surface area A of particles moving inside a closed container, such that a vacuum is nothing but

the absence of particles like molecules and atoms. Historically, the standard pressure was set to $101.325\,\mathrm{kPa} = 1\,\mathrm{atm}$, which is the atmospheric pressure at sea-level, although it was replaced in 1982 by the International Union of Pure and Applied Chemistry (IUPAC) and NIST[37] to be $10^5\,\mathrm{Pa} = 1\,\mathrm{bar}$. This shift to more smooth values explains why the unit of Pa (= *Pascal*) is rather uncommon giving way to the unit $\mathrm{mbar} = 10^2\,\mathrm{Pa}$. Over the years of research, eight regimes of vacuum have been defined by different regimes of vacua listed below[38].

Table 3: Different regimes of vacua.

Vacuum quality	presssure [mbar]	pressure [atm]
Atmospheric pressure	1.013×10^2	1
Low vacuum	$< 1 \times 10^2$	$< 9.87 \times 10^{-1}$
Medium vacuum	$< 1 \times 10^0$	$< 3 \times 10^{-2}$
High vacuum	$< 1 \times 10^{-4}$	$< 9.87 \times 10^{-7}$
Very high vacuum	$< 1 \times 10^{-7}$	$< 9.87 \times 10^{-10}$
Ultra-high vacuum	$< 1 \times 10^{-10}$	$< 9.87 \times 10^{-13}$
Extreme ultra-high vacuum	$< 1 \times 10^{-13}$	$< 9.87 \times 10^{-16}$
Perfect/Absolute vacuum	0	0

The regimes of interest in this cold atoms experiment range from atmospheric pressure to Ultra-high vacuum (UHV) .

3.4.2 *Pumping Down the Vacuum*

Although advanced technologies and a variety of different pumping mechanisms have been developed and are still researched, no pump has the ability to pump a volume from atmospheric pressure down to UHV, which is why several pumps at different stages must be deployed.

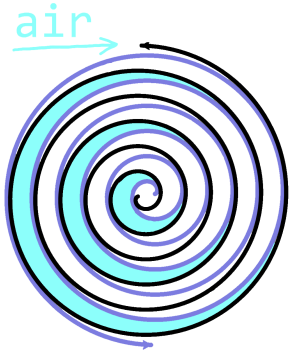

Figure 15: Air being moved and compressed between the two interleaving spirals (black and purple).

The vacuum **pre- or roughing pump** is the nXDS displacement pump from Edwards[3]. It belongs to the sub-type of scroll pumps, which remove the atoms and molecules by physically displacing them with help of two interleaving scrolls (see Figure 15).

3 https://www.edwardsvacuum.com/en

Molecules are sucked in at the outermost loop of the spirals and are moved continuously towards the centre while being compressed with every turn. An exhaust at the centre removes the atoms completely from the pump. Its peak pumping speed is $1140\,l/h = 0.32\,l/s$ and may reach an ultimate vacuum of 7×10^{-3} mbar[39].

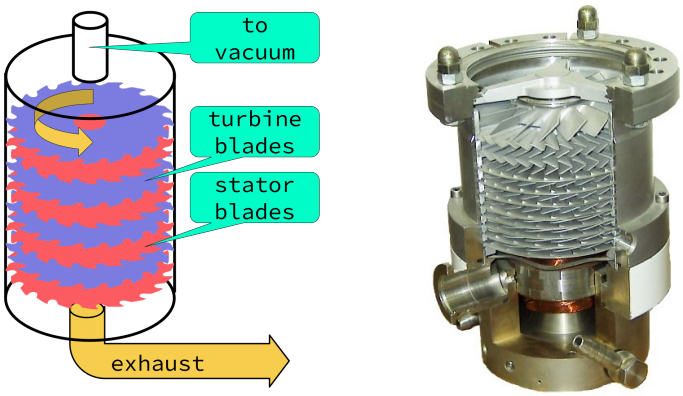

Figure 16: Schemtatic (a) and real-life picture (b) of a turbo pump. Image taken from [40]

At pressures of $p_{roughing} \sim 10^{-3}$ mbar the **turbo molecular pump** can be started, which reaches pressures of $p_{turbo} \sim 10^{-6}$ mbar within half of an hour. Turbo molecular pumps consist of several layers of quickly rotating and static fans with ten or more blades, which repeatetly hit the molecules remaining inside the volume. By this, the momentum of the moving blades is transferred to the particles moving them further into the pump creating a flux of molecules towards the exhaust. A schematic and real-life picture of a turbo pump is shown in Figure 16.

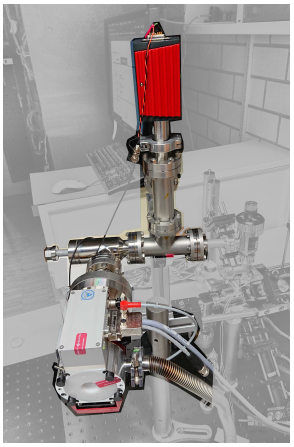

Figure 17: Pumping stage as used on the 2D-MOT chamber.

Both, the roughing and the turbo molecular pump, are connected in series and share the same exhaust. Together with a pressure gauge (PG) make up the pumping stage, which is also shown in Figure 17. The red part is the PG and the grey component at the bottom is the turbo pump with a hose connecting it to the scroll pump not shown in the figure.

To reach the regime of UHV, a controlled heating up of the vacuum chambers must be performed, since residual particles remain not only freely inside the chamber but are also sticking to the walls and may even have infiltrated inside their material. This desorption and

diffusion mechanism in which the molecules are released from the surface and the inner structure of the material and disturb the vacuum is contributing to a process called outgassing[41]. Furthermore, vapourisation of the bulk material itself and permeation, the movement of molecules from the external atmosphere through the material, add to outgassing of the material. Heating up the material to high temperatures of sometimes up to $T = 500\,^{\circ}C$, removes impurities already present and additionally reduce the overall outgassing rate of the vacuum set-up material in total. This process is also-called *bake-out*, however fails to remove the light Hydrogen molecules completely. More specifics of this procedure are given later in this chapter.

The next and final bit of work is performed by an **ion pump**, whose working principle is as follows: A cloud of electrons is stored around an anode, which ionises the atoms and molecules in the gas. These ions are then accelerated towards a chemically active cathode, which not only attracts them but binds them into the material itself. Typical electrical potentials are of the order of $V_{ion} \sim 5\,kV$. It enables the removal of the majority of the remaining H_2 molecules up to a partial pressure of $p_{H_2} \approx 4 \times 10^{-8}\,mbar$.

3.4.3 *Vacuum Set-Up*

In this section, we will go through the whole vacuum set-up depicted in Figure 18. For the three most important components - the 2D-MOT, main, 3D-MOT/science chamber - separate schematics are given in Figure 19.

① : The experiment starts with a source of atoms at the 2D-MOT chamber, where an oven provides the ^{39}K isotope. In our case, it consists of a small cup, which is filled with a 5 g ingot and is connected with a short nipple at the bottom of the 2D-MOT chamber. Both, cup and nipple, are enclosed with band heaters, which can be controlled independently. Setting the oven temperature allows us to have control over the potassium vapour pressure inside the vacuum chamber and determines the amount of atoms being captured by the trap. The nipple above or oven nozzle has to be heated as well such that the potassium atoms do not stick to the walls of the narrow tube. The according experimental data will be discussed in a later chapter (see Chapter 4).

② : The 2D-MOT chamber features four ConFlat®[4] (CF) 16 viewports allowing the 2D-MOT beams and their retroreflections to overlap at the centre.

The push beam pointing towards the main chamber is directed towards the cloud of atoms through a CF40 viewport. Although reduced in size, the whole 2D-MOT chamber design as well as using permanent magnets instead of coils for the magnetic field generation

4 *ConFlat* is an international registered trademark of Varian, Inc.

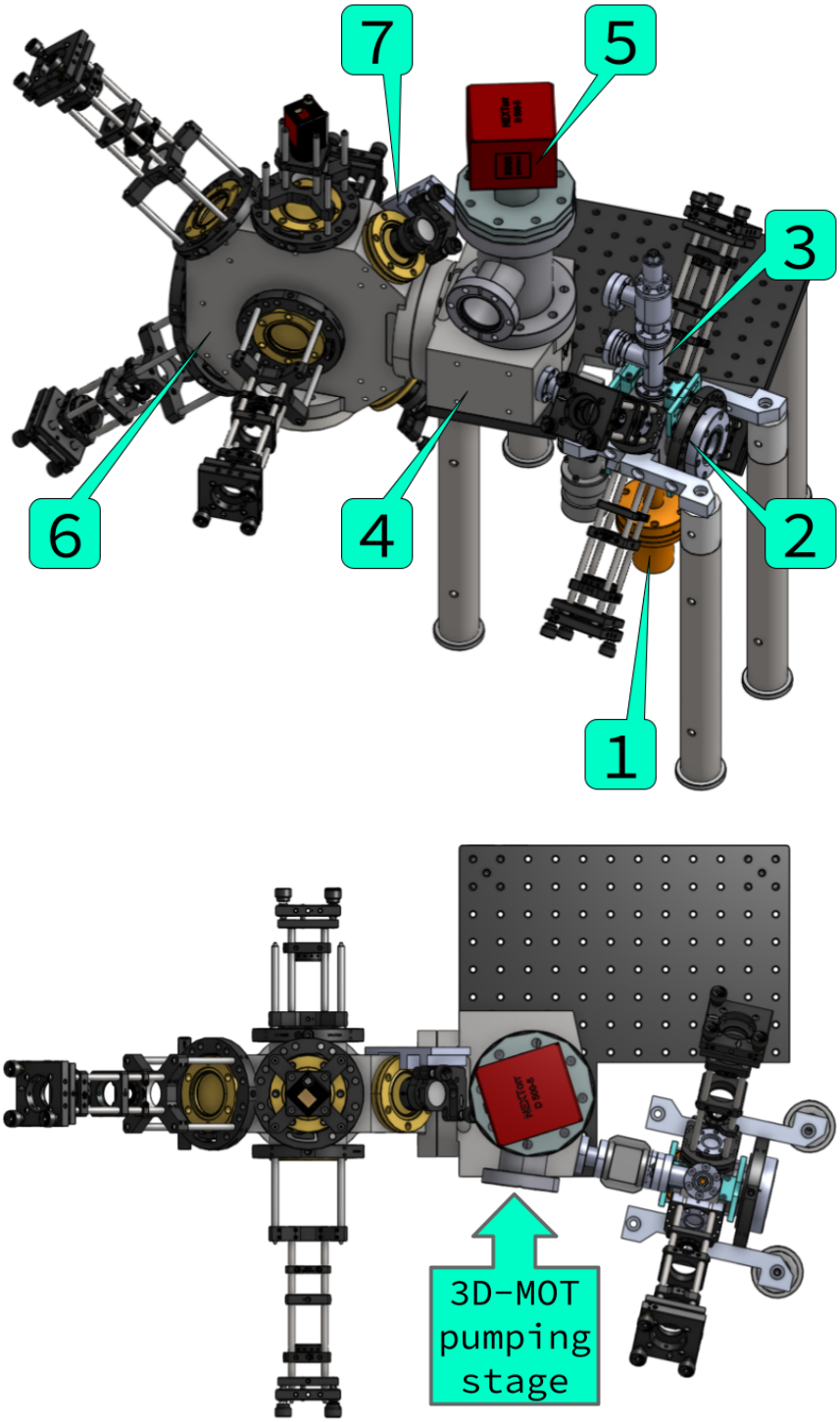

Figure 18: Schematics of the full vacuum set-up.

was inspired by the work of a group of scientists in Trento, Italy[42] and the SoPa experiment in Heidelberg[43][44].

③ : On top, a small tee junction connects the chamber to an angle valve and a CapaciTorr®5 pump. The angle valve serves as a gate be-

5 *CapaciTorr* is an international registered trademark of SEAS Getters S.p.A.

tween the 2D-MOT chamber and the pumping stage, which is closed as soon as the pumping down process is completed and the pumping stage can be removed. This pump is passive as it is activated once and then neither powered by any electrical or chemical supply. After the thin protective layer (primarily oxides and carbides) is removed by a heating process lasting two hours and reaching temperatures of $T_{CT} = 450\,^{\circ}C$, it catches mainly H_2 (20 l/s) and CO (15 l/s) molecules by binding them into the active getter medium consisting of an alloy of Iron (Fe), Vananium (V) and Zirconium (Zr).

Unfortunately, the CapaciTorr did not show the desired results. After closing the valve between the tee to the pressure gauge and the two pumps, pressure started to rise indicating that the passive CapaciTorr pump did not work properly. Even after reactivating it twice, it did not show any satisfactory results such that the pumping stage stayed connected to the 2D-MOT set-up during the whole time. A leak was ruled out after a throughout leak search.

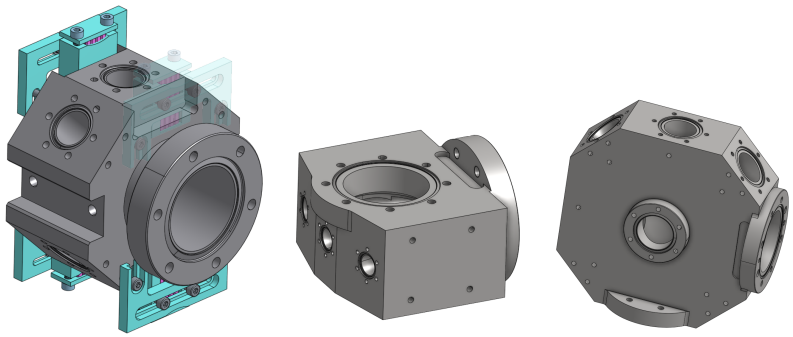

(a) 2D-MOT chamber (b) Main chamber (c) 3D-MOT chamber

Figure 19: Two views of the three vacuum chambers. The pumping stage is not included to provide a more clear picture.

④ : The main chamber has three CF16 input flanges of which only one is currently occupied by the ^{39}K 2D-MOT and one CF63 flange on top and the far side opposite to the opening for the 2D-MOT chamber. The first connection pointing upwards connects the main chamber to an ion getter pump (⑤, NEXTorr D500 by SEAS Getters S.p.A.[6]; Aluminium (Al), Vananium (V) and Zirconium (Zr) getter) with a H_2 pumping speed of 500 l/s[45]. Its electrical potential is $V_{ion} = 5\,kV$.

⑥ : The science or 3D-MOT chamber is where the experiments take place. It is an octogonal shaped titanium chamber with eight CF40 viewports and one CF63 connector to be mounted on the main chamber. This allows for several different beam configurations for the three-dimensional cold atom trapping to be realised and creates other opportunities for e. g. optical dipole trapping. A CF63 opening at the bottom is currently closed with a blind flange, which could be replaced by a viewport to even further expand imaging as well as

6 https://www.saesgetters.com/

trapping options. Furthermore, there are several options for imaging the trapped atoms inside the chamber such that the most suitable viewport may be used.

As stated above, to reach the required low pressures for UHV, even contaminations within the chamber material have to be considered. This excludes water absorbing materials like aluminium or impure alloys. Furthermore, the importance of uniform and predictable magnetic fields forbids the usage of magnetic and easily magnetizable metals even for small components like screws and washers. For the different chambers (2D-MOT, main chamber, science chamber) we therefore chose titanium whereas stainless steel (SST 304) was considered to be sufficient for standard vacuum components like pipes, junctions, blinds and viewport frames. Compared to stainless steel, titanium has a lower density[46][47], what makes the partially thickly walled chambers lighter, and outgassing rate, which will be elaborated in Section 3.4.5.

3.4.4 *Quantifying the Vacuum*

While pumping down the 2D-MOT chamber only a simple pressure gauge was available, a proper residual gas analyzer (RGA100 by Scientific Instruments GmbH[7]) was added to the pumping stage during the attachment of the main and science chamber. This time, the pumping stage was connected with an angle valve at the horizontal opening of the tee on top of the main chamber (only hinted in Figure 18). The RGA is a mass spectrometer with a very sensitive detector and is able to give an account on the remaining gas molecules inside the vacuum. It typically detects the following molecules with high accuray : H_2, H_2O, CO, N_2, CO_2, He, Ar, O_2 (already roughly sorted by their abundance with H_2 being the largest in number). For example, N_2 with 28 amu (atomic mass units) can be detected at partial pressures as low as 6.6×10^{-11} mbar[48]. Larger molecules like those for pump oils can be detectes as well. Because of its high sensitivity, it may only operate at pressures lower than 1.3×10^{-4} mbar.

With an electron source, the remaining molecules are first ionised and then accelerated towards a detector unit while filtered according to their mass-to-charge ratio. The ions hitting the analyzer create a current at a certain spot on the detection surface, which is therefore a measure of the respective amount of molecules. In Figure 20 below, two screenshots of the gas spectrum, that is the partial pressures of the different molecules are shown.

7 https://www.si-gmbh.de/

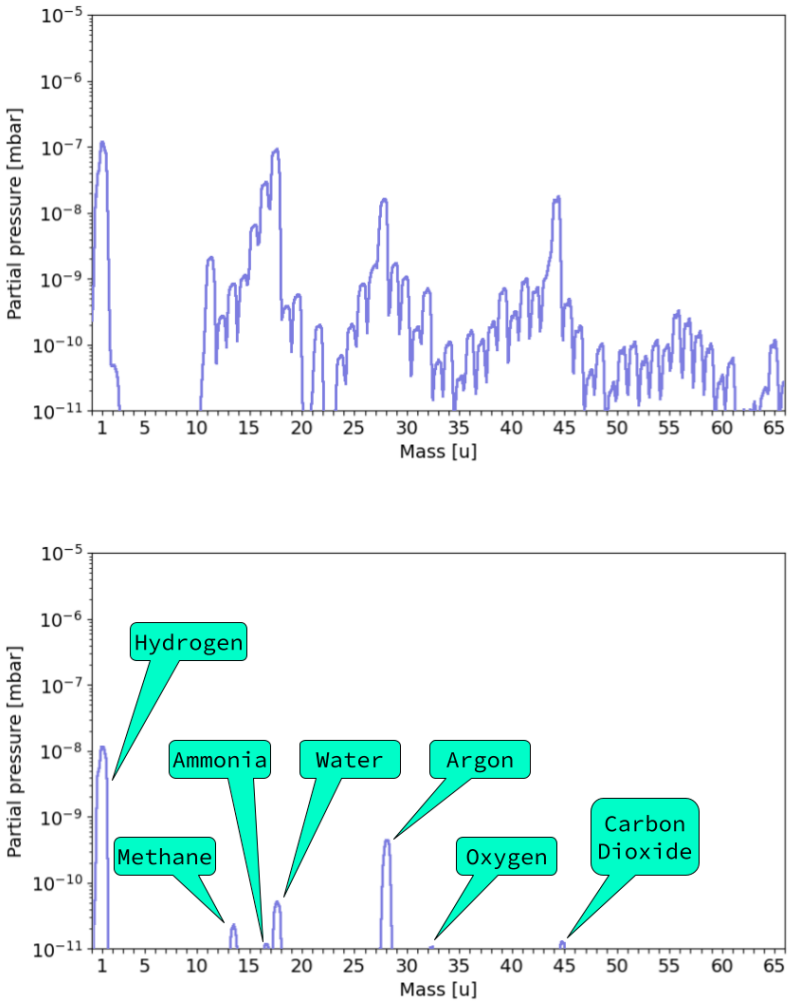

Figure 20: Gas spectrum before (top) and after (bottom) completion of the pumping down process.

3.4.5 *Bake-Out*

After assembling the vacuum, a bake-out was performed. The maximum temperature ratings of the viewports is $T_{max} = 200\,°C$, so that the heating process was limited to approximately 195 °C. While some components of the set-up like the chambers and tubes could technically be exposed to more heat, others like the pumps have a lower upper limit.

The challenge is to heat up the whole system up uniformly such that the impurities do not accumulate at colder spots. This can be achieved by wrapping the vacuum components with long heating bands and cover them with tin foil. Longer bands are advantageous because they distribute the same heat to several places at once and the outer layer of tin foil serves as an effective isolation, keeping the warmth inside instead of radiating it out into the environment. Due

to the low heat conductance of titanium and stainless steel, wrapping a layer of tin foil tighly around the vacuum components before deploying the heating bands contributes to an uniform heating as well.

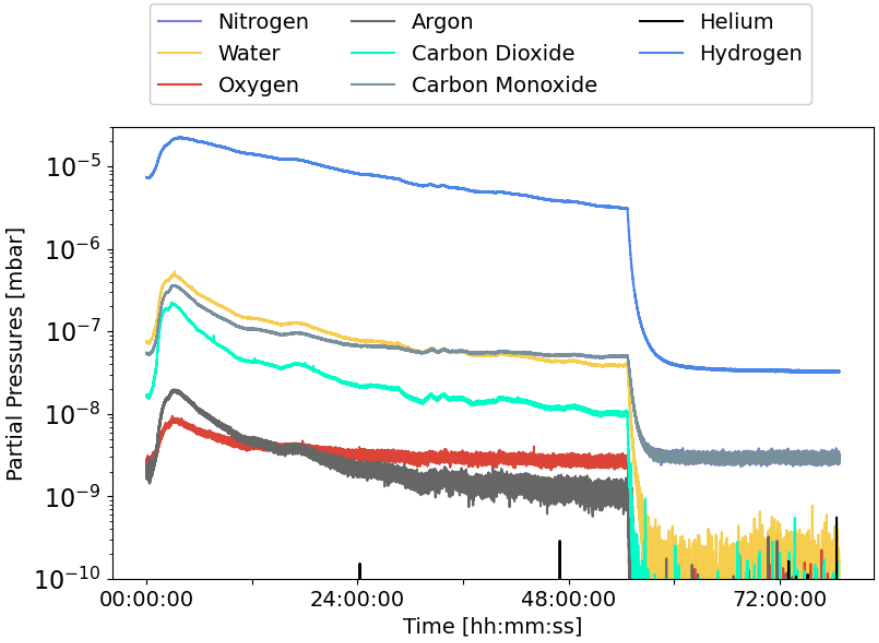

Figure 21: Partial pressures for the most abundant molecules during bake-out.

As a result, pressure firstly rises as more and more molecules are removed from the walls and cast into the empty volume of the system. In Figure 21, this process is shown by increasing partial pressures of several types of molecules. After about 55 h, the heating was turned off and the pressures decreased down to two orders smaller than before for Hydrogen and even lower values for the other gases.

After some time, almost all molecules are pumped out and the partial pressures fall below their initial values and the bake-out process is completed. This time as well as the temperature varies from experiment to experiment since they have different components with specific heat resistances, in general however, baking to higher temperatures is more beneficial. The time required to perform a successful bake out falls exponentially with higher temperatures such that in our case, the bake out took place over the duration of about five days. The final pressure as measured by a sensor integrated into the ion pump was $2 \times 10^{-10}\,\mathrm{mbar}$.

In Figure 22, the significantly decreasing outgassing rates for stainless steel after heat treatment at different temperatures for different times are shown. For titanium, the outgassing rate without heat treatment is $\dot{Q} = 1.0 \times 10^{-8}\,\mathrm{mbar\,s \cdot l/s \cdot cm^2}$, although baking at $T = 150\,^{\circ}\mathrm{C}$ for 20 h can reduce this value to the order of $\dot{Q} \sim \times 10^{-14}\,\mathrm{mbar \cdot l/s \cdot cm^2}$[50].

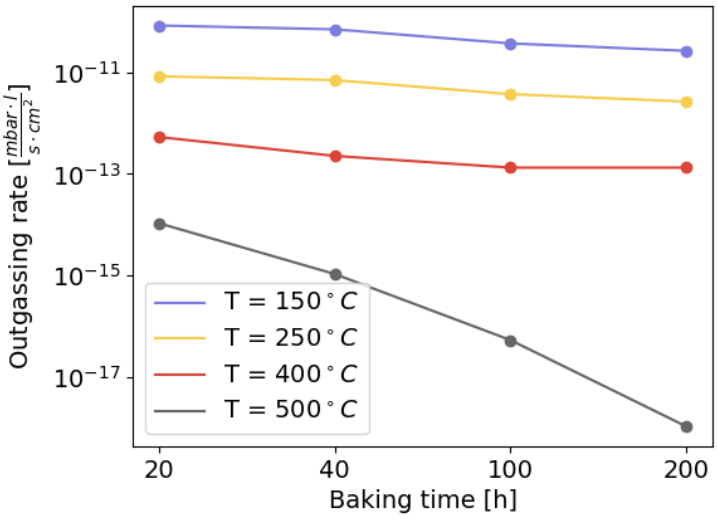

Figure 22: Final outgassing rates for stainless steel after different heat treatment. Data taken from[49].

3.4.6 *Design Considerations*

Before the vacuum system described above has any experimental usage, several prerequisites must be satisfied. Firstly, the prepared laser beams must be deployed to the respective vacuum chambers and directed through the correct viewports. Secondly, anti-*Helmholtz* coils for the magnetic field generation must be mounted at the 2D-MOT and 3D-MOT chambers. Furthermore, the oven as well as the short nipple guiding the atoms towards the 2D-MOT chamber (nozzle) must be heated in some way or other. All solutions to these requirements are described in the following.

OPTICAL CAGE SYSTEM To bring the laser power and frequencies into the vacuum system, we use a cage flange adapter[8](①), which can be mounted on viewports and therefore features an inner diameter conforming to standard CF sizes. For the two-dimensional MOT as well as for the three-dimensional case, they partially had to be cut into shape such that they do not coincide with adjacent adapters or vacuum components. An exampleratory set-up is shown in Figure 23a.

After the laser beam is coupled out of the fibreport ①, it is transformed into circular polarised light by means of a $\lambda/4$-waveplate (in a rotatable mount ③ and collimated with a $f = 75\,mm$ AR (anti-reflection)-coated lens ④ suitable for potassium light. The resulting beam size is about $12\,mm$ for the 2D-MOT as well as for the 3D-

8 https://www.thorlabs.de/newgrouppage9.cfm?objectgroup_id=9125

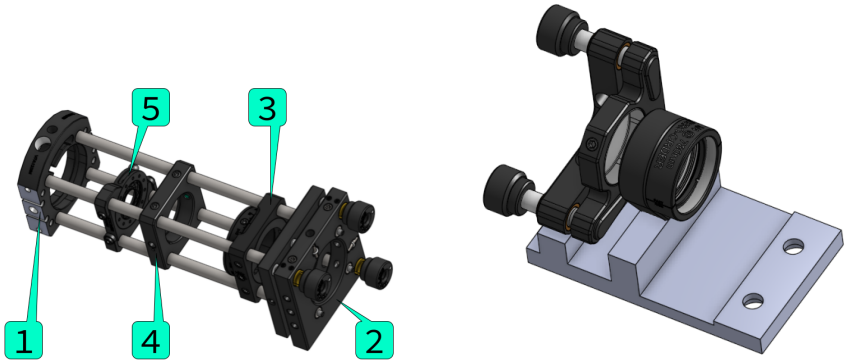

Figure 23: Left : An optical cage system as used in the experimental set-up. Right : Small holder plate to mount the retro-optics.

MOT. An optional iris ⑤ may decrease the beam size, which helps with aligning the incoming and retro-reflected beams and changing the size of the cloud of trapped atoms. The only differences between the systems for the 2D- and 3D-Mot were the set-ups for the retro-reflected beams. Whereas for the 2D-MOT another set of cage systems was deployed, this was impossible for the two vertical beams of the 3D-MOT. The tee connecting the ion pump and the main chamber would collide with the cage systems such that a small aluminium part was designed to hold the mirror and $\lambda/4$-plate (see Figure 23b and ⑦ in Figure 18).

MAGNETIC FIELD GENERATION Because of spatial restrictions, convenience and stability, strong permanent magnets were used to generate the magnetic field required for the 2D-MOT. They are fitted into a specially designed magnet mount, which can be mounted on the 2D-MOT chamber itself and allows for corrections along two directions. While this solution was sufficient for the first stage, for the 3D-MOT, the conventional solution of two anti-*Helmholtz* coils were used. The coils are of a rectangular shape with $12\,\mathrm{cm} \times 14\,\mathrm{cm}$ as side length giving it an effective radius of $R = 8.2\,\mathrm{cm}$ and are driven with a current of $I_{coils} = 20\,A$. A model calculation of the generated fields was already shown in Figure 4.

HEATING AND TEMPERATURE Wherever a heating clamp is applied, a thermocouple element serves as feedback towards a PID controller loop also running on an Arduino (Tctrl). The output voltage of the PID is connected to a NS80, a low-noise phase-angle dimmer[51], which in turn controls the power given to the metal band heaters. Last but not least, a third type of Arduino (THsen) is built into the optical rack and serves as a "weather station". It measures the humidity and temperature inside the rack.

3.4.7 *Challenges in Miniaturisation*

While other experiments have large-sized experimental tables at their disposal, the restriction for the vacuum set-up to fit into a 19-inch rack was by far the most challenging aspect. For this means, everything had to be miniaturised starting from the vacuum chambers and other vacuum components to the parts connecting the optical elements to them. CF16 flanges are not uncommon, however mounting and fixing them requires quick handiwork with minuscule tools and fidgety parts. Working angles of only a part of a screw turn and anticipating the reduced stability of bolts while working with gloves makes handling those small-sized components rather tedious. Additionally, the total volume flowing through narrow pipes and junctions is more limited than for broader openings.

3.5 SUMMARY

After understanding the basic laser principles in Chapter 2, the device used in this thesis was presented at the beginning of this chapter. Lasers might be a powerful tool, it is necessary however to control them according to the specific needs of the ^{39}K atoms. First of all, it must be locked to avoid frequency shifts having an impact on the cold atoms experiment. Furthermore, the two seperate laser tables, which are connected via a pm fibre, create pump and cooling light for a two and three dimensional MOT as well as a push beam, which transfers the cloud of atoms captured in the 2D-MOT chamber to the science chamber.

The second half of this chapter gave a brief introduction to vacuum systems in general as well as some exemplary descriptions of the working principle of scroll, turbo and ion-getter pumps. Beginning with the 2D-MOT chamber as the starting point of the vacuum set-up, the upper sections guided through the several additions made at a later stage.

4

MAKING A COLD QUANTUM GASES EXPERIMENT TRANSPORTABLE

This thesis so far went through the fundamental building blocks of a cold atoms experiment. Starting with basic atom light interaction, we first saw how to trap atoms with specific laser light and how we obtain it by locking a laser and subtle frequency manipulation of the output. We also had a look at the vacuum system on which the laser beams are actually deployed and trap the atoms first of all in the 2D-MOT and then - being transferred there by means of another light beam (push) - to the science chamber. In this chapter, we will discuss the outermost layer of the mechanical experimental set-up, which are the two 19-inch racks, by going through both of them in a separate section. Furthermore, a brief overview over the remote experimental control will be given. Aiming to make this cold atom experiment compact and transportable, both, the remote control system and the mobile racks, are essential.

4.1 SET-UP IN A 19-INCH RACK SYSTEM

As already introduced in the first chapter of this thesis, the set up of a cold atoms experiment in a 19-inch rack system is motivated by a number of reasons. First of all, it saves a lot of space by avoiding broad optical table and instead making use of vertical capacities. This is not beneficial for smaller laboratories only, but is making use of available room more efficiently in general. Also many electronic components are already designed to fit into 19-inch racks as industry is always on the look-out for standardised norms. All devices can be overviewed at a glance and connections between signal generators, amplifiers, read-out boards etc. can be established quickly while saving extra long cables hanging across the room. A good example for this technology are server rooms, where all devices can be easily added, removed and accessed without every time having to take into account the individual dimensions and positions of plugs and ports of every device. Furthermore, server rooms offer the highest internet security measures, perfect networking connections and a temperature as well as vibration controlled environment. Usually are equipped with powerful air conditioning systems, which not only cool down processors and hard drives, but prevent larger fluctuations in temperature and humidity in general to ensure smooth operation. Protection against vibration is accomplished by throughout planning of the location of these facilities (e. g. not too close to busy roads) and

building design (e. g. sound-proof doors or acoustical panelling and tile ceiling). In the following subsections, more details and emerging challenges for the two specific rack types will be reviewed.

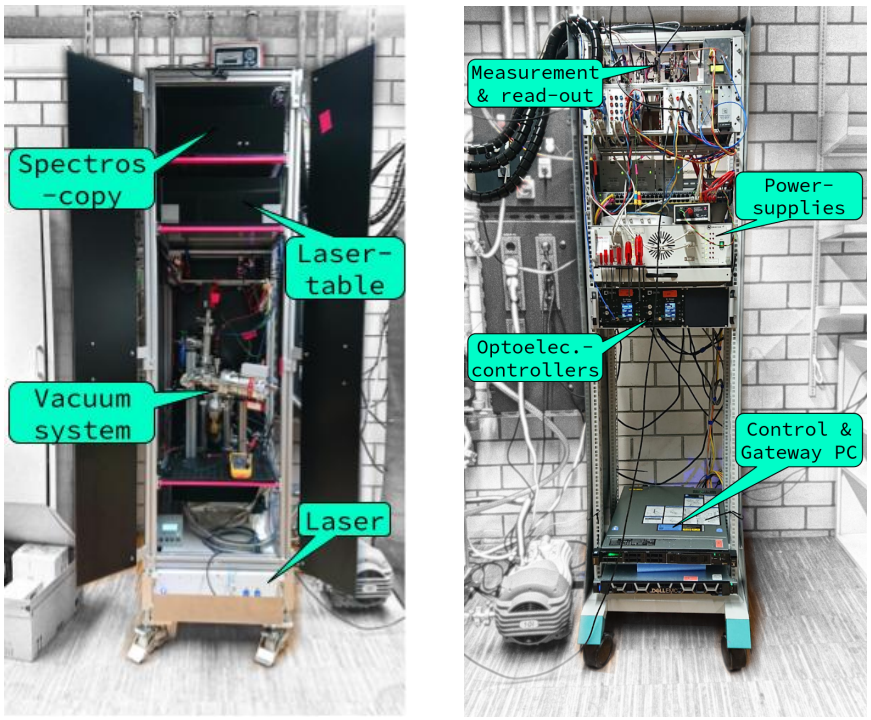

Figure 24: Optics and electronics rack.

4.1.1 *Optics Rack*

A frame is mounted on top of four blockable wheels of about $d \approx 15\text{cm}$ diameter. It consists of six robust item profiles, which make up a structure of $210\text{cm} \times 50\text{cm} \times 60\text{cm}$ total height, width and depth. The whole rack is rather static so no suspensions are protecting the frame base and connected parts from vibrations of the floor. Furthermore, depending on how one places the different modules inside the rack, its centre of gravity may eventually lie quite up high. We planned to equip the rack with four sliding drawers, whose vertical position may be chosen freely. While three drawers were sufficient for 2D-MOT stage of our experiment, the advancement of the experiment towards a 3D-MOT instituted the necessity to add another drawer, hosting a second laser table.

On the very top, a drawer with a breadboard, hosts the spectroscopy set-up discussed in Chapter 3. The two main reasons for this decision were that it was one of the modules which was well-aligned and ready for usage at a very early stage as well as that the band heaters constantly running at 65 °C may otherwise affect the other optics in a negative way. Directly below, the first laser table drawer is equipped

with the double pass for the 2D-MOT and a splitting set-up to obtain two balanced, fibreized outputs to be deployed on the vacuum. It also contains an in-coupler, which couples light to the second drawer via a short fibre. On the second drawer, the double pass for the push beam and the 3D-MOT as well as a coupling set-up to split and couple the 3D-MOT light into three fibres are located. The drawer meant for the vacuum system and the laser are sitting at the very bottom and are only separated by a 3U-heightened frame[1], which is equipped with the THsen, a PDmon board and a breakout panel providing voltages of $\pm 5, \pm 12, \pm 15\,\mathrm{V}$. These are oftentimes used to power our home-built photodiodes or frequency counters for the AOM VCO boards.

The optical drawers are laser protected with DiBond[2] and may be pulled out to their full extent depthwise. Three larger DiBond plates protect the sides and the back whereas two slimmer plates serve as a double door with two handles at the front. Because the protective mantle is mounted to the outer side of the item profiles, a space of about 4cm on the left and right hand side allows for guiding cables and fibres with help of cable management clips, cable binders and velcro cable ties.

CHALLENGES Aligning the first laser table (2D-MOT beam paths) on the breadboard, which was already mounted inside the optics rack with only a restricted space at hand, was a difficult task to undertake. Therefore, we aligned the optics of the second laser table (3D-MOT and push beam paths) on the breadboard outside the o-rack and put it in afterwards. With this, smaller adjustments had still to be made, but this was far more feasible than aligning with difficult working angles and continuously standing on a ladder. Also avoiding cables to be squashed by the drawers or getting entangled and keeping in mind to leave enough spare fibre and cable length to let the drawers be pulled out and pushed in smoothly was challenging. The most difficult part, however, was to design the vacuum system in such a way that it would fit into the comparatively small space given by the optic-rack's dimensions. A thorough discussion for this was already presented in Chapter 3.

4.1.2 *Electronics Rack*

The o-rack was designed to be roughly of the same size as the e-rack, which was bought from an external company and is therfore conform to industry standards ($60\,\mathrm{cm} \times 60\,\mathrm{cm} \times 190\mathrm{cm}$). Its frame does not consist of item profiles but thinner metal bars, which proved to be not as resistant to vibrations (e. g. shaking the rack). Once again, we list all items from the top to the bottom:

1 $1\mathrm{U} = 44.45\,\mathrm{mm}$ - it is a standardised size for vertical elements in 19-inch racks
2 Two PVC plates with an aluminium layer glued in between

1. A 19-inch rack frame (see Figure 25) into which the current amplifier, RedPitaya, three Tctrls and amplifiers for the RF signal directed to the AOMs are built-in.

2. Another rack frame with two breakout panels, a voltage adder board and three voltage controlled oscillator (VCO) boards providing the RF signals for the AOMs.

3. A rackable ethernet switch with PoE (power over ethernet) function with the NS80 mounted on a rail screwed at the rear rack posts.

4. A stable, low-noise power supply delivers the different voltages ($\pm 5, \pm 12, \pm 15$ V) to the several breakout boards.

5. Down on the lowest levels of the rack, the gateway and experimental control PCs are mounted.

CHALLENGES The main difficulty here lay in securing all devices for the transportation and unplugging incoming and outgoing signal cables to the o-rack and reconnecting them after reaching the HRI. Three cable hoses helped with organising different streams of cables (e. g. those for receiving and delivering signals were separated from mere power cables) and keeping them together in smaller bunches. In the current set-up, these connectors allow for a maximal distance between the two racks of about 1 m.

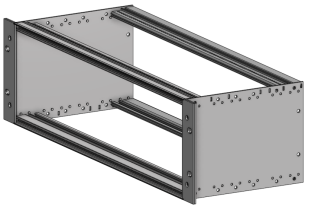

Figure 25: 3U rackframe.

4.2 REMOTE CONTROL

The last crucial part for completing the task of making our cold atoms experiment independent of the locality, a well designed experimental control system had to be built up. Django, a python-based REST (**Re**presentational **s**tate **t**ransfer) framework for web developement, already includes many pre-implemented functions and classes such that a user is motivated to write re-usable apps instead of reprogramming individual applications for every single usage. The idea was to create a uniform platform to access and control the smaller lab devices like the several Arduino boards or our RedPitaya laser locker. To give an impression, a screenshot of the GUI (graphical user interface) is shown in Figure 26 and the full code can be looked up on GitHub[3]. The panels for the Tctrl Arduino shown in the screenshot allows to

3 https://github.com/synqs/DjangoControlServer

change the PID values, look at a specific timespan by zooming in the plots as well as looking up values in an up-to-date table. If only certain parameters are of interest, they can be individually displayed or kept hidden. Additionally, the sleeptime, which is the time interval at which the devices are asked for data, can be set. The server itself runs on the local control PC, which can be reached through a VPN server running on the gateway PC, but a more detailed view on the network configuration will be given in the subsequent subsection.

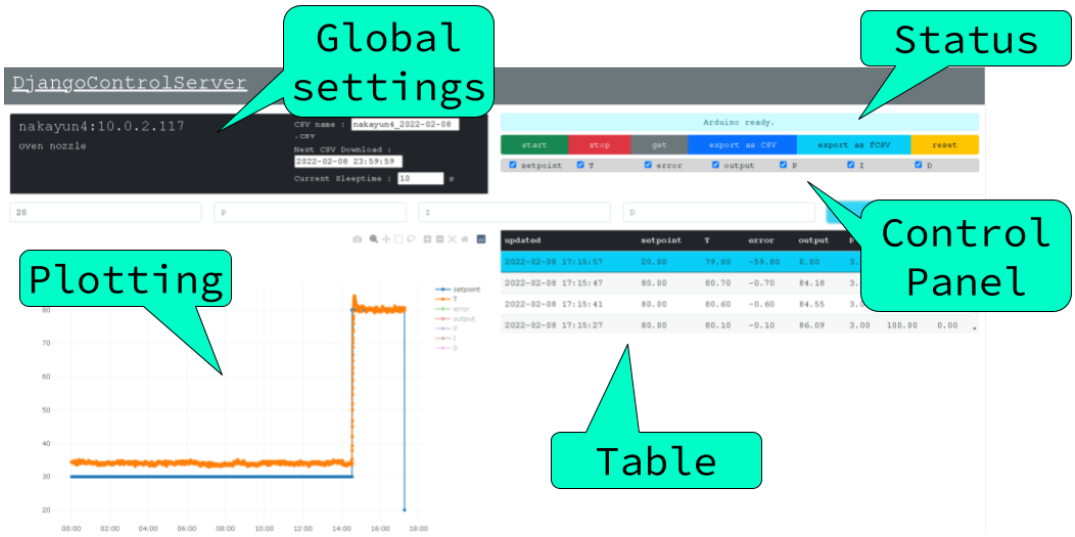

Figure 26: Screenshot of the GUI inside a web browser.

As our team is using SLACK[4], a messaging platform available for almost all operating systems, for daily communication, a bot embedded inside a jupyter notebook also keeps track of the laser lock. If the laser falls out of lock, a message is sent into a designated channel with the time of incidence attached. Since all data from the DjangoControlServer is backed up in a cloud-based, file hosting service, one can look at the other data points around that time frame afterwards and try to find connections.

4.2.1 *Network Configuration*

Even though data centres may provide ideal environmental conditions for running an experiment such as the one discribed in this thesis, but they have one big disadvantage: Understandibly, only devices providing the same hyper-secure user authentication and certification systems are allowed access to their internal networks. As this would have required an IT-specialist to think of such a scheme for the NaKa. Instead, we came up with another solution, which involves a mobile LTE modules providing access to the internet through a pay-as-you-go sim card flatrate.

4 https://slack.com/

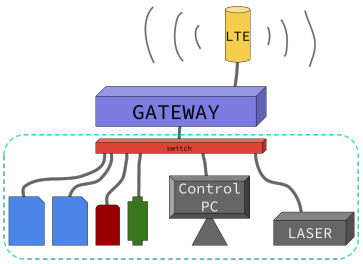

Figure 27: Network Configuration.

This LTE module is directly connected to the gateway PC, which serves as a "gate" to the world wide web and regulates in- and out-going traffic and is connected to the switch. It also hosts the private sub-network so all devices have a static IP address looking like this : 10.0.2.xxx. Such a sub-network does not only protect the laboratory devices from unwanted data transfer to the outside but also does not interfere with the already configured, surrounding networks. A schematic is shown in the Figure 27. Here, the LTE module (yellow) connects the gateway PC (purple) to the internet, which in turn accesses the internal private network (dotted green line).

To get access to the control PC and the gateway PC itself, one needs to authenticate at a virtual proxy network (VPN) server portal configured with the help of Apache Guacamole®[5], which allows for establishing a GUI connection as well as a simple terminal session. Guacamole is a remote desktop gateway, which supports protocols like VNC, RDP and SSH and does not require a user to install a browser plug-in or client. This allows access from any PC connected to the internet with a web browser.

4.3 SUMMARY

The purpose of this chapter was to have a detailed look on how the goal of making a cold atoms experiment transportable and remotely controllable. Going through both racks step-by-step, not only their particular outer structure but also all experimental units and devices mounted inside were exploited. Challenges in compressing a full experiment into two 19-inch racks were discussed as well.

The last section of this chapter gave an impression on how the experiment can be controlled and data collected fully remotely.

5 https://guacamole.apache.org/

5 COOLING AND TRAPPING OF ^{39}K

In this chapter the experimental data of the two- and three-dimensional trap will be presented and discussed.

5.1 TIMELINE AND METHODS OF MEASUREMENT

This section is dedicated to present the remaining details of the set-up not mentioned before. As soon as the optical and electric rack frame were built-up, we started equipping them with power supplies, lab devices, optical breadboards and frequency generators. Starting in March 2021, a small DFB (distributed feedback) butterfly diode providing about $P_{DFB} \sim 40\,mW$, served as a preparational substitute and helped with aligning the spectroscopy and the 2D-MOT double pass. Furthermore, some changes had to be made on the laser table for example deploying the *Galilean telescope* and exchanging coupling lenses to adjust for the different beam size.

The vacuum for the 2D-MOT including bake-out and activation of the CapaciTorr pump was prepared even before the currently operating laser arrived, which replaced the small DFB diode. After this was established, the necessary optics were added to the vacuum chamber using a cage system, which is mounted onto the vacuum viewports. November 3rd as a date for transport to the collaborating Honda Research Center in Offenbach (Main), the hunt for the 2D-MOT signal started two weeks before, reserving some time to prepare both racks to be moved out of the laboratory. Since a 2D-MOT signal was quickly found, the remaining time could be used for further optimization.

For three weeks, the experiment resided in a small server room at the research centre during which some particular measurement series were taken to characterise the system in addition to observing the experiment around the clock. Before Christmas break 2021, rework as well as preparations for the next steps were made on the returning set-up. With the beginning of the new year and the arrival of the until then missing main and science chamber, the vacuum system was extended by these components.

In its current state, the experiment fulfills all requirements to produce a three-dimensional MOT. It was not yet realised in the frame of this thesis, but allows for further investigation.

5.1.1 *Data Acquisition*

Next to the photodiode (PD) detecting the signal of the probe beam on the saturated absorption spectroscopy table, another is put opposite of the second PBS. It accounts for remaining polarisation fluctuations not eradicated by the first PBS, which is referred to as *dump* beam/signal. The two split-up coupling paths for the 2D-MOT are intersected with a pick-off plate (cover slips for micro slides used in microscopy) which cast a probe beam unto a PD (*pick-off* signal). These measures were taken to get an impression on the stability of the optical rack system being exposed to vibrations and the whole process of transportation. Because the paths are split by means of a PBS, this too offers another opportunity to account for polarization fluctuations. In addition, as those two paths exhibit the highest optical power, it was convenient to pick-off some light there. Currently two PDs are mounted behind the mirrors inside the cage system of the 2D-MOT's retro-reflected beams to monitor their stability.

All of those PDs are fed into a voltage monitor board (PDmon), which is an electrical wafer card with an Arduino Yún mounted on top. Five channels can be observed. The Arduino may only measure voltages between $\Delta V_{yun} = 0 - 5\,V$, however a voltage divider allows it to cover the whole PD range of up to $V_{PD} = 12\,V$.

The other two types of arduinos (Tctrl and THsen) were already introduced in Section 3.4.6, with which the heating of the heating clamps at the spectroscopy and the oven are controlled and the environmental temperature and humidity are observed.

The fluorescence signal of the atoms trapped in the MOT is observed with a Mako G-030B (a monochromatic CMOS camera by Allied Vision[1]). It features a resolution of $644 \times 484\,px$ and a maximum image bit depth of 12 bit, meaning that the final image is given in 12 shades of grey. The fluorescence of the atoms on the dark background is summed over every pixel (for the 2D-MOT an image of approximately $25 \times 25\,px$ was used).

5.2 REMOTE COLD ATOM TRAPPING

Before assembling the whole vacuum system including the main and science chamber, the first goal was to achieve the two-dimensional magneto-optical trap. Because the second laser table generating the light for the 3D-MOT and the push was not yet set up, the full power of the high-power output could be sent into the double pass for the 2D-MOT. In order to make the signal hunting efficient, the oven and the oven nozzle were heated up to $T_{oven} = 80\,°C$ and $T_{nozzle} = 100\,°C$ respectively. Both MOT beams had a power of

1 https://data2.manualslib.com/pdf4/94/9340/933947-allied_vision/mako_g030bc.pdf?830b9c4f3f430cf035b8926fc7c0970f

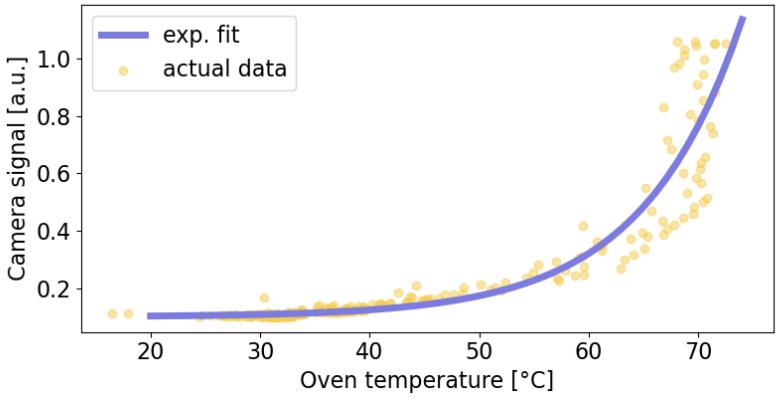

(a) Signal amplification compared to the signal strength at $T = 30\,°C$.

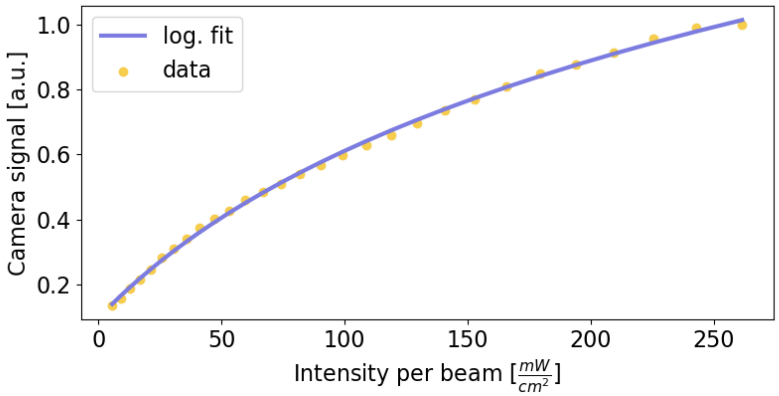

(b) Signal amplification compared to the signal strength at maximum power.

Figure 28

$P_{2D} \approx 135\,mW$ with a beam diameter of $d_{2D} = 8\,mm$. Once the signal was acquired, different settings were tried out as well. Since our signal was so pronounced, that a cloud of atoms was detectable with both, oven and nozzle heaters, turned off or in the process of cooling down overnight even. Experimental data for these tests is shown in the next section, which were all accumulated during the stay of the experiment at the Honda Research Institute.

EXPERIMENTAL DATA In the graph above (Figure 28a), a measurement of the 2D-MOT signal versus the oven temperature is shown. The whole process of heating the vacuum parts up to the set value of $T_{oven,set} = 70\,°C$ and $T_{nozzle,set} = 90\,°C$ and cooling down to their initial values of $T_{oven,ini} = 30\,°C$ and $T_{nozzle,ini} = 50\,°C$ took about $\Delta t = 2\,1/2\,h$. One can see that the camera signal increases exponentially with increasing temperatures as more potassium atoms are emitted from the ingot inside the oven. As a consequence, more atoms may be captured by the trap.

In sub-Figure 28b a measurement of the camera signal depending on the laser power is shown as well. Here the relation is of logarithmic nature : Even though more and more photons are sent towards the atoms, at some point no more atoms can be addressed and the signal saturates.

During its stay at a server room at the Honda Research Institute, several observables were monitored all the time. As an example, the whole dataset of measurements over the timespan of a whole day is shown in Figure 27.

The two racks were standing in a small server room at Offenbach with a strong air conditioning system. It did not have a PID regulation for temperature control and instead turns on at full power as soon as temperature reaches an upper limit. When the lower bound is measured, it turns off completely until the next cooling down is initiated by rising room temperatures. This behaviour can be seen in almost all observables as well especially in the 2D-MOT fluorescence (Figure 28d).

Next to these short time fluctuations, overall changes are visible in subfigure b, d and f as well. They can be explained by the natural day and night cycle and the accompanying environmental influences. Seemingly, this server room was not as suitable as we thought it might be, however the room was currently also occupied by rather insensitive, simpler electronics, which are not influcenced by the impactful air conditioning system. Also the different modes of the day-night heating cycle of the building should not affect the devices already present. Server rooms are a suitable environment still, however the necessary requirements to run a potentially more sophisticated and sensitive experiment should be considered first. As it is, the server room at Honda was sufficient for running the 2D-MOT and in every way convenient to test the electronical, optical and technical set-up of our cold atoms experiment.

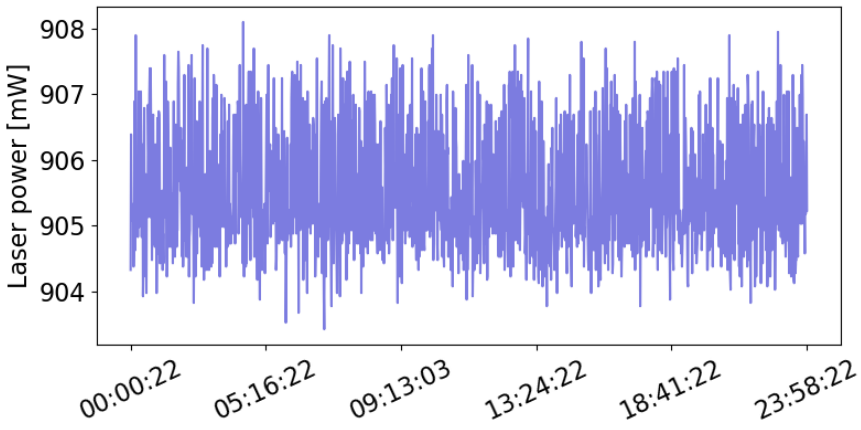

(a) Laser power fluctuations at P = 1 *W* as measured with the laser's built-in sensor

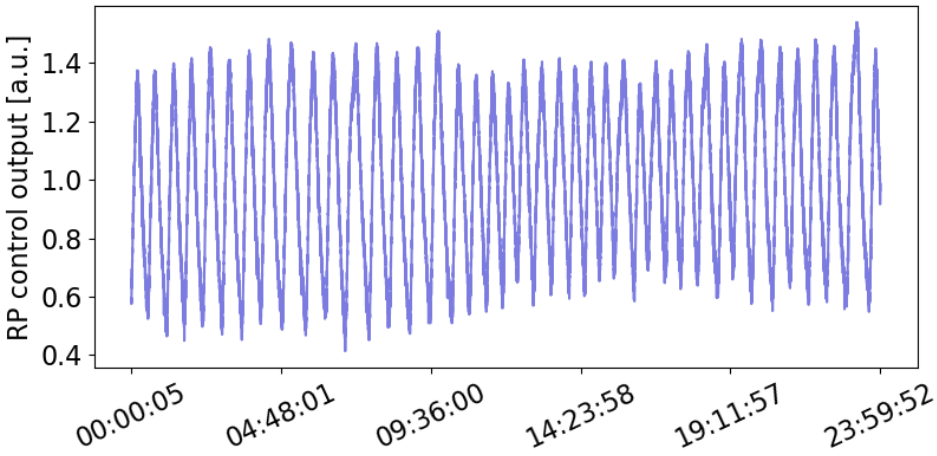

(b) Relative fluctuations of the laser control output (PID)

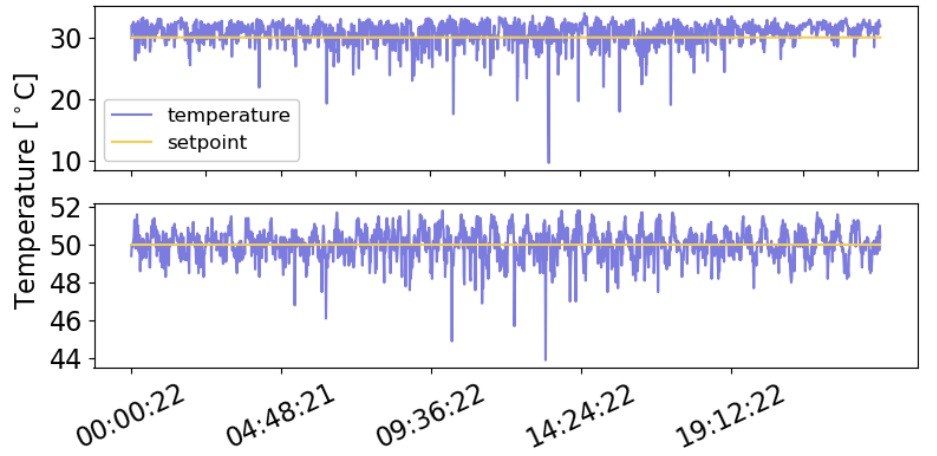

(c) Temperature and setpoint of oven (top) and nozzle (bottom) heating clamps

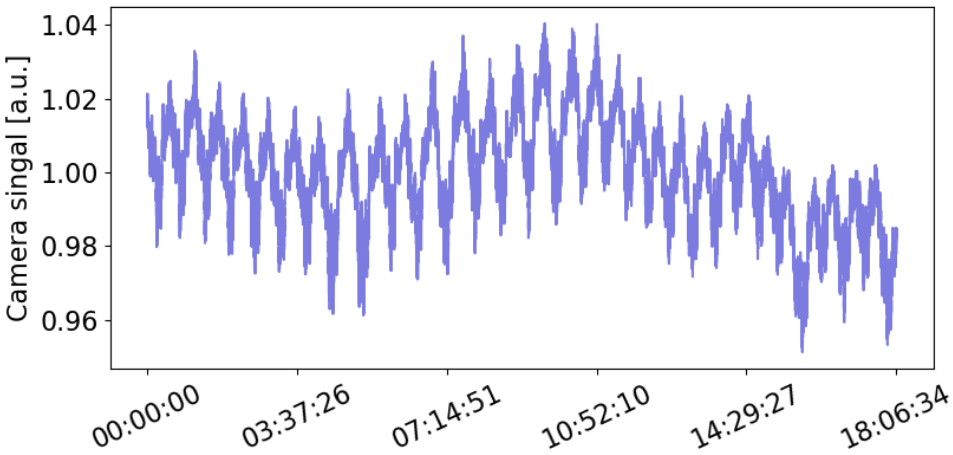

(d) Fluctuations of the 2D-MOT signal

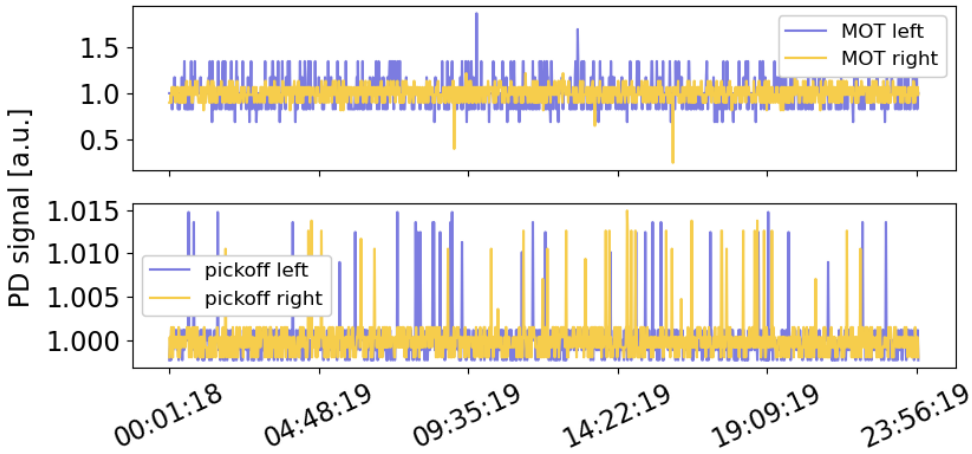

(e) Fluctuations of the 2D-MOT beams at the chamber (top) and on the table (bottom)

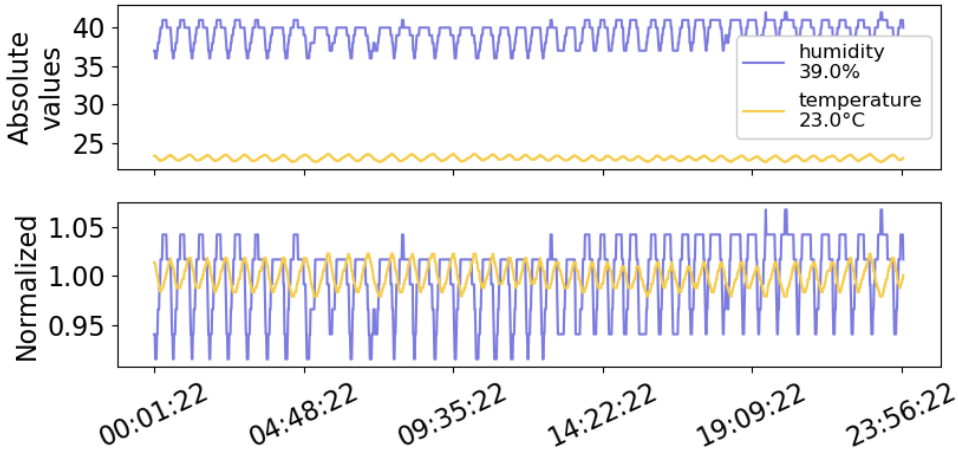

(f) Total values (top) and relative fluctuation (bottom) of temperature and humidity inside the o-rack

Figure 27: Dataset for a whole day.

6 CONCLUSION AND OUTLOOK

This final chapter will summarize all experimental data, gained experiences and give a brief look on how the experiment could be advenced still.

WHAT WE HAVE LEARNED SO FAR... All in all, the ambitious task to achieve a two-dimensional magneto-optical trap, which could be transferred to, monitored at and controlled from a complete remote location within the timespan of less than a year, was accomplished successfully. Furthermore, the was even time to extend the system to a runnable 3D-MOT within the given timeframe. Also the novel approach to design the experiment to be operational within the boundaries of a 19-inch rack frame provided us with new insights:

First and foremost, we did not think that the experiment, especially the optics, proved to be so stable even after the $11/2\,\mathrm{h}$ trip from Offenbach to Heidelberg. After unwrapping the racks and powering the laser and the other devices, the 2D-MOT signal could be restored without making any adjustments. Only some smaller tweaks further improved the fluourescence signal. Also after having performed the packing progress for the first trip once, enabled us to save some time for doing the same thing for the journey back. During times of operation, the laser lock was also very stable and kept the laser in lock even though we shook the o-rack and blocked the laser beam for a short period of time.

Additionally, the convenience to store a once well aligned optical assembly into a shelf where it is protected from dust and light noise (e. g. from other light sources inside the laboratory) was quite convincing. And even though one sees no need or benefit from transporting an experiment to another location, it might be useful to have the possibility to move it around inside the laboratory or the hallway of the facility into another room.

...AND WHAT WE CAN STILL DREAM OF. First of all, a three-dimensional magneto-optical trap should be achieved. Next to enhancing fibre coupling efficiencies and optical alignment, more time is needed for "signal hunting", which is the rather arbitrary tuning of several parameters in the hope of observing a cloud of fluorescing atoms on the camera.

As shown in the vacuum section Chapter 4, the vaccum system offers many options for further additions. One option would be to deploy diople beams to the 3D-MOT inside the science chamber, which

is another atom trapping scheme not discussed here (for more information on this, referr to e. g. [52]). With this, tweezer experiments as perfomed by other cold atom groups[53][54][55] could be run on the NaKa as well.

Furthermore, the other CF16 flange on the main chamber may be used to connect another 2D-MOT chamber, introducing a second atomic species like Sodium or Lithium, as already implemented by the SoPa or NaLi experiment in a very similar manner[43][44]. This offers new possibilities on investigating in two species cold atom physics[56].

Regarding the racks itself, a central cooling system could help stabiling the o-rack in temperature even further while a system of fans deployed on the e-rack may help the electronics to keep cool under continuously operation. Also introducing spring-suspended wheels for the optical rack might make more sensitive experiment possible or improve the results currently achieved.

BIBLIOGRAPHY

[1] Niels Bohr. In: *Philosophical Magazine*. 6th ser. 26 (1913), pp. 1–25.

[2] E. Schrödinger. "Die gegenwärtige Situation in der Quantenmechanik." In: *Naturwissenschaften* 23.48 (1935), pp. 807–812. ISSN: 1432-1904. DOI: 10.1007/BF01491891. URL: https://doi.org/10.1007/BF01491891.

[3] W. Heisenberg. "Über den anschaulichen Inhalt der quantentheoretischen Kinematik und Mechanik." In: *Zeitschrift für Physik* 43.3 (1927), pp. 172–198. ISSN: 0044-3328. DOI: 10.1007/BF01397280. URL: https://doi.org/10.1007/BF01397280.

[4] A. L. Schawlow and C. H. Townes. "Infrared and Optical Masers." In: *Phys. Rev.* 112 (6 1958), pp. 1940–1949. DOI: 10.1103/PhysRev.112.1940. URL: https://link.aps.org/doi/10.1103/PhysRev.112.1940.

[5] K. B. Davis, M. O. Mewes, M. R. Andrews, N. J. van Druten, D. S. Durfee, D. M. Kurn, and W. Ketterle. "Bose-Einstein Condensation in a Gas of Sodium Atoms." In: *Phys. Rev. Lett.* 75 (22 1995), pp. 3969–3973. DOI: 10.1103/PhysRevLett.75.3969. URL: https://link.aps.org/doi/10.1103/PhysRevLett.75.3969.

[6] Stephen Eckel, Daniel S Barker, James A Fedchak, Nikolai N Klimov, Eric Norrgard, Julia Scherschligt, Constantinos Makrides, and Eite Tiesinga. "Challenges to miniaturizing cold atom technology for deployable vacuum metrology." In: *Metrologia* 55.5 (2018), S182–S193. DOI: 10.1088/1681-7575/aadbe4. URL: https://doi.org/10.1088/1681-7575/aadbe4.

[7] Henry Charles Fleeming Jenkin. *Reports of the committee on electrical standards*. British Association for the Advancement of Science, 1873.

[8] J.W. Horton and W.A. Marrison. "Precision Determination of Frequency." In: *Proceedings of the Institute of Radio Engineers* 16.2 (1928), pp. 137–154. DOI: 10.1109/JRPROC.1928.221372.

[9] Time Serive Department. "Leap Seconds." In: (Mar. 2015). URL: http://tycho.usno.navy.mil/leapsec.html.

[10] I. I. Rabi, J. R. Zacharias, S. Millman, and P. Kusch. "A New Method of Measuring Nuclear Magnetic Moment." In: *Phys. Rev.* 53 (4 1938), pp. 318–318. DOI: 10.1103/PhysRev.53.318. URL: https://link.aps.org/doi/10.1103/PhysRev.53.318.

[11] J. V. Louis Essen L.; Parry. "An Atomic Standard of Frequency and Time Interval: A Cæsium Resonator." In: *Nature* 176.4476 (1955), pp. 280–282. ISSN: 1476-4687. DOI: 10.1038/176280a0. URL: https://doi.org/10.1038/176280a0.

[12] Dörscher, N Huntemann, R Schwarz, R Lange, E Benkler, B Lipphardt, U Sterr, E Peik, and C Lisdat. "Optical frequency ratio of a $^{171}Yb^{+}$ single-ion clock and a ^{87}Sr lattice clock." In: *Metrologia* 58.1 (2021), p. 015005. DOI: 10.1088/1681-7575/abc86f. URL: https://doi.org/10.1088/1681-7575/abc86f.

[13] *Transportable Clock*. Apr. 2016. URL: https://www.ptb.de/cms/en/ptb/fachabteilungen/abt4/fb-43/ag-432.html?type=#maincontent_forschung_header.

[14] A. Einstein. "Grundgedanken der allgemeinen Relativitätstheorie und Anwendung dieser Theorie in der Astronomie." In: *Sitzungsberichte* 315 (1915).

[15] J. C. Hafele and Richard E. Keating. "Around-the-World Atomic Clocks: Predicted Relativistic Time Gains." In: *Science* 177.4044 (1972), pp. 166–168. DOI: 10.1126/science.177.4044.166. eprint: https://www.science.org/doi/pdf/10.1126/science.177.4044.166. URL: https://www.science.org/doi/abs/10.1126/science.177.4044.166.

[16] Tobias Bothwell, Colin J. Kennedy, Alexander Aeppli, Dhruv Kedar, John M. Robinson, Eric Oelker, Alexander Staron, and Jun Ye. "Resolving the gravitational redshift within a millimeter atomic sample." In: (2021). arXiv: 2109.12238 [physics.atom-ph].

[17] Jacopo Grotti et al. "Geodesy and metrology with a transportable optical clock." In: *Nature Physics* 14.5 (2018), pp. 437–441. ISSN: 1745-2481. DOI: 10.1038/s41567-017-0042-3. URL: https://doi.org/10.1038/s41567-017-0042-3.

[18] Kai Bongs et al. "Development of a strontium optical lattice clock for the SOC mission on the ISS." In: *Comptes Rendus Physique* 16.5 (2015). The measurement of time / La mesure du temps, pp. 553–564. ISSN: 1631-0705. DOI: https://doi.org/10.1016/j.crhy.2015.03.009. URL: https://www.sciencedirect.com/science/article/pii/S1631070515000602.

[19] S. B. Koller, J. Grotti, St. Vogt, A. Al-Masoudi, S. Dörscher, S. Häfner, U. Sterr, and Ch. Lisdat. "Transportable Optical Lattice Clock with 7×10^{-17} Uncertainty." In: *Phys. Rev. Lett.* 118 (7 2017), p. 073601. DOI: 10.1103/PhysRevLett.118.073601. URL: https://link.aps.org/doi/10.1103/PhysRevLett.118.073601.

[20] Migue Orszag. *Atom–Field Interaction: Semiclassical Approach*. 3rd ed. Springer Nature, 2019. Chap. 2. ISBN: ISBN 978-3-319-29035-5. DOI: 10.1007/978-3-319-29037-9.

[21] Claude Cohen-Tannoudji, Bernard Diu, and Franck Laloë. 2nd ed. John Wiley & Sons, 2019. ISBN: 3527345531.

[22] Rudolf Grimm, Matthias Weidemüller, and Yurii B. Ovchinnikov. "Optical dipole traps for neutral atoms." In: *Advances in Atomic, Molecular, and Optical Physics* 42 (Dec. 2000), p. 95. DOI: 10.1016/S1049-250X(08)60186-X.

[23] Wofgang Demtröder. *Emission und Absorption elektromagnetischer Strahlung durch Atome. Atome, Moleküle und Festkörper*. 5th ed. Springer Spektrum, Berlin, Heidelberg. Chap. 7. ISBN: 978-3-662-49093-8. DOI: https://doi.org/10.1007/978-3-662-49094-5.

[24] Christian Doppler. "Ueber das farbige Licht der Doppelsterne und einiger anderer Gestirne des Himmels." In: (1842). URL: https://de.wikisource.org/wiki/\%C3\%9Cber_das_farbige_Licht_der_Doppelsterne_und_einiger_anderer_Gestirne_des_Himmels.

[25] V. S. Letokhov, V. G. Minogin, and B. D. Pavlik. "Cooling and capture of atoms and molecules by a resonant light field." In: *Soviet Journal of Experimental and Theoretical Physics* 45 (1977). Provided by the SAO/NASA Astrophysics Data System, p. 698. URL: https://ui.adsabs.harvard.edu/abs/1977JETP...45..698L.

[26] J. Dalibard and C. Cohen-Tannoudji. "Laser cooling below the Doppler limit by polarization gradients: simple theoretical models." In: *J. Opt. Soc. Am. B* 6.11 (1989), pp. 2023–2045. DOI: 10.1364/JOSAB.6.002023. URL: http://www.osapublishing.org/josab/abstract.cfm?URI=josab-6-11-2023.

[27] T. G. Tiecke. "Properties of Potassium." In: (June 2019). URL: https://tobiastiecke.nl/archive/PotassiumProperties.pdf.

[28] Thomas Jefferson National Accelerator Facility Office of Science Education. Jan. 2022. URL: https://education.jlab.org/itselemental/ele019.html.

[29] Jabez Mcclelland, A. Steele, B. Knuffman, Kevin Twedt, A. Schwarzkopf, and Truman Wilson. "Bright focused ion beam sources based on laser-cooled atoms." In: *Applied Physics Reviews* 3 (Oct. 2015). DOI: 10.1063/1.4944491.

[30] Claude N. Cohen-Tannoudji. "Nobel Lecture: Manipulating atoms with photons." In: *Rev. Mod. Phys.* 70 (3 1998), pp. 707–719. DOI: 10.1103/RevModPhys.70.707. URL: https://link.aps.org/doi/10.1103/RevModPhys.70.707.

[31] "Lasers." In: *Fundamentals of Photonics*. John Wiley & Sons, Ltd, 1991. Chap. 14, pp. 494–541. ISBN: 9780471213741. DOI: https://doi.org/10.1002/0471213748.ch14. eprint: https://onlinelibrary.wiley.com/doi/pdf/10.1002/0471213748.ch14. URL: https://onlinelibrary.wiley.com/doi/abs/10.1002/0471213748.ch14.

[32] MUQUANS. *High-power frequency-stabilized laser system*. 2019. URL: https://www.muquans.com/wp-content/uploads/2019/03/muquans_generic_laser.pdf.

[33] T. Kessler, C. Hagemann, C. Grebing, T. Legero, U. Sterr, F. Riehle, M. J. Martin, and J. Chen L.and Ye. "A sub-40-mHz-linewidth laser based on a silicon single-crystal optical cavity." In: *Nature Photonics* 6.10 (2012), pp. 687–692. ISSN: 1749-4893. DOI: 10.1038/nphoton.2012.217. URL: https://doi.org/10.1038/nphoton.2012.217.

[34] "Acousto-Optics." In: *Fundamentals of Photonics*. John Wiley & Sons, Ltd, 1991. Chap. 20, pp. 799–831. ISBN: 9780471213741. DOI: https://doi.org/10.1002/0471213748.ch20. eprint: https://onlinelibrary.wiley.com/doi/pdf/10.1002/0471213748.ch20. URL: https://onlinelibrary.wiley.com/doi/abs/10.1002/0471213748.ch20.

[35] Suha Mousa Alawsi and Lubaba Abdul Kareem AL-Janabi. In: *International Journal of Science and Research* 7 (3 2018). ISSN: 2319-7064. URL: https://www.ijsr.net/archive/v7i3/ART2018754.pdf.

[36] Gooch & Housego. 2022. URL: https://gandh.com/product-categories/acousto-optic-modulators/.

[37] A. D. McNaught and A. Wilkinson. *Compendium of Chemical Terminology*. 2nd ed. Blackwell Scientific Publications, 1997. ISBN: 0-9678550-9-8. DOI: https://doi.org/10.1351/goldbook.

[38] John F. O'Hanlon. *Chapter 1 : Vacuum Technology*. John Wiley & Sons, Feb. 2005.

[39] Edwards. Jan. 2022. URL: https://www.edwardsvacuum.com/content/dam/brands/edwards-vacuum/edwards-website-assets/scientific-vacuum/documents/brochures/Edwards-nXDS-Dry-Scroll-Pump-Brochure-3601-0088-01.pdf.

[40] Liquidat. *A cut-through turbomolecular pump model. The different rotor sizes and grain sizes can clearly be seen.* 2005. URL: https://commons.wikimedia.org/wiki/File:Cut_through_turbomolecular_pump.jpg.

[41] Rebecca Grinham and Dr Andrew Chew. "A review of outgassing and methods for its reduction." In: *Applied Science and Convergence Technology* 26.5 (2017), pp. 95–109.

[42] G. Lamporesi, S. Donadello, S. Serafini, and G. Ferrari. "Compact high-flux source of cold sodium atoms." In: *Review of Scientific Instruments* 84.6 (2013), p. 063102. DOI: 10.1063/1.4808375. eprint: https://doi.org/10.1063/1.4808375. URL: https://doi.org/10.1063/1.4808375.

[43] Jan Kilinc. "Starting a Na-K experiment for simulating quantum many-body phenomena." 2019. URL: https://www.synqs.org/publication/thesis/kilinc-2019/.

[44] Lilo Höcker. "Building up a modular Na-K quantum gas experiment." 2019. URL: https://www.synqs.org/publication/thesis/hoecker-2019/.

[45] SEAS Getters S.p.A. 2022. URL: https://www.saesgetters.com/sites/default/files/NEXTorr\%20D\%20datasheets.pdf.

[46] William M. Haynes. *Handbook of Chemistry and Physics*. 93rd ed. CRC, 2012. ISBN: 9780429111228. DOI: https://doi.org/10.1201/b12286.

[47] thyssenkrupp Materials (UK) Ltd. 2022. URL: https://www.thyssenkrupp-materials.co.uk/stainless-steel-304-14301.html.

[48] Scientific Instruments GmbH. 2022. URL: https://www.si-gmbh.de/wp-content/uploads/2021/02/RGAc_SI.pdf.

[49] Manoj Gupta, Abhinav Priyadarshi, and Ziauddin Khan. "Hydrogen in Stainless Steel as Killing Agent for UHV: A Review." In: *Materials Today: Proceedings* 2 (Dec. 2015), pp. 1074–1081. DOI: 10.1016/j.matpr.2015.07.011.

[50] Masatoshi Takeda, Hiroki Kurisu, Setsuo Yamamoto, Hamazo Nakagawa, and Katsunobu Ishizawa. "Hydrogen outgassing mechanism in titanium materials." In: *Applied Surface Science* 258.4 (2011), pp. 1405–1411. ISSN: 0169-4332. DOI: https://doi.org/10.1016/j.apsusc.2011.09.092. URL: https://www.sciencedirect.com/science/article/pii/S0169433211014942.

[51] FG-Elektronik. 2012. URL: https://asset.conrad.com/media10/add/160267/c1/-/de/000510699DS02/datasheet-510699-fg-elektronikns-80built-in-dimmer-phase-speed-controlna-dimmer.pdf.

[52] Rudolf Grimm, Matthias Weidemüller, and Yurii B. Ovchinnikov. "Optical Dipole Traps for Neutral Atoms." In: *Advances in Atomic Molecular and Optical Physics* 42 (2000), pp. 95–170. DOI: 10.1016/S1049-250X(08)60186-X. arXiv: physics/9902072 [physics.atom-ph].

[53] Edwin Pedrozo-Peñafiel et al. "Entanglement on an optical atomic-clock transition." In: *Nature* 588.7838 (2020), pp. 414–418. ISSN: 1476-4687. DOI: 10.1038/s41586-020-3006-1. URL: https://doi.org/10.1038/s41586-020-3006-1.

[54] L.-M. Duan, E. Demler, and M. D. Lukin. "Controlling Spin Exchange Interactions of Ultracold Atoms in Optical Lattices." In: *Phys. Rev. Lett.* 91 (9 2003), p. 090402. DOI: 10.1103/PhysRevLett.91.090402. URL: https://link.aps.org/doi/10.1103/PhysRevLett.91.090402.

[55] Thomas Chalopin. "Optical superlattices in quantum gas microscopy." In: *Nature Reviews Physics* 3.9 (2021), pp. 605–605. ISSN: 2522-5820. DOI: 10.1038/s42254-021-00357-8. URL: https://doi.org/10.1038/s42254-021-00357-8.

[56] Alexander Mil. "Experimental realization of U(1) gauge invariance in ultracold atomic mixtures." In: (2020). URL: https://www.synqs.org/publication/thesis/mil-2020/.

Let the morning bring me word of your unfailing love,
for I have put my trust in you.
Show me the way I should go,
for to you I entrust my life.
- PSALMS 143:8

ACKNOWLEDGEMENTS

On one of these last pages, I want to thank everyone who made this this thesis possible in the first place.

First of all, I want to thank **Fred** for being my supervisor since my bachelor thesis in 2020. He did not only motivate and inspire me by his fascination of physics and seeing the ”bigger picture”, but also made me feel like we could really accomplish something with our work.

Yannick and **Lilo**, who really put much effort into the NaKa and worked hard, although they were involved in several other projects as well, deserve my respect. Without you guys, the NaKa would have never come to life! Lilo’s humor and her practial way of thinking and doing made my day times and again and I will remember her as the first face I ever saw of this group in real life (remember? You gave me that small innocent RedPitaya on a fresh February day...).

Rohit and **Jan** were always there for me when in need of theoretical and practical advise. I enjoyed your company for more than two years already.

Lisa also was a great help especially in the last phase of my master’s studies. She sometimes spend a lot of her time with me in the lab, shared her experiences and supported me when I was frustrated with bad fiber coupling.

Commander Andy taught me how things get done (speed and power, but sometimes caution) and showed how to stay strong through times of struggling with our experiments.

I also want to thank **Mr. Martìn-Amendral**, who went through pages and pages of incorrect order forms and misunderstandings caused by me in the first place. **Dagmar** and **Christiane** from the office also were kinder to me than they had to be, giving a hand when having to deal with the paper work.

Finally, I want to thank my new-found friends in Heidelberg and those elsewhere. Especially my parents and my siblings, whom I love and who did not only support in the past two years during the NaKa was built, but also did so my whole life long.

During the past year, I oftentimes did - and I sadly still do - wake up and the first thoughts on my mind and words on my lips are "LORD, thank you for this morning and this day, but why did you make it happen anyways?" I was asking this question or rather mak-

ing this accusation regarding global hunger, deadly wars, climate crisis and seemingly endless suffering of the lost and most vulnerable. The whole creation is sighing and seeks redemption from this mess we have created ourselves. But then I remember that we are redeemed already. Jesus came into this world as a mere human, though he was God, and became sin, though he was holy. Why? Because he loved us more than anything. Why? So that he may be glorified through us.

So I do not exactly know why he made this particular day. Sometimes, I am still full of doubt and internal struggles, although listening to his Spirit and seeking answers in his word. But this I know and these shall be the last word of this thesis :

"But as truly as I live, all the earth shall be filled with the glory of the LORD." - Numbers 14:21

DECLARATION

Ich versichere, dass ich diese Arbeit selbstständig verfasst habe und keine anderen als die angegebenen Quellen und Hilfsmittel benutzt habe.

Heidelberg, February 2022

Ingrid Maria Dippel